2007-05-25

Design of a Noninvasive System for the Evaluation of Collagen Scaffolds Using MRI

Stuart C. Howes
Worcester Polytechnic Institute

DESIGN OF A NONINVASIVE SYSTEM FOR THE EVALUATION OF COLLAGEN SCAFFOLDS USING MRI

A thesis submitted to the faculty of the
WORCESTER POLYTECHNIC INSTITUTE
in partial fulfillment of the requirements for the
Degree of Master of Science in
Biomedical Engineering

by

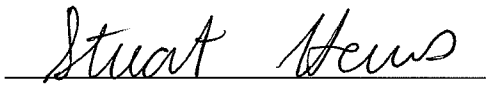

Stuart Howes
May 2007

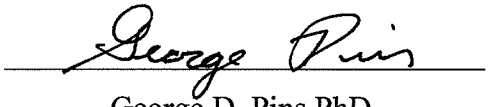

George D. Pins PhD.
Associate Professor, Major Advisor
Biomedical Engineering Department
Worcester Polytechnic Institute

Christopher H. Sotak PhD.
Professor and Department Head
Biomedical Engineering Department
Worcester Polytechnic Institute

Glenn Gaudette PhD.
Assistant Professor
Biomedical Engineering Department
Worcester Polytechnic Institute

Abstract

Collagen implants are widely used in clinical practice and are an active area of research. The continued development of collagen-based implants often relies on histological techniques to fully evaluate the host response post implantation. These destructive, end-point analyses limit the rate that data can be obtained from samples. Magnetic resonance imaging has the potential to non-invasively monitor the remodeling of collagen scaffolds. In this study, scaffolds prepared from insoluble bovine collagen, with varied and predictable tissue responses were implanted in rats and evaluated using both histological and MRI techniques. Treatment of scaffolds with a carbodiimide crosslinker was found to slow the degradation and cellular infiltration into the scaffolds compared to uncrosslinked scaffolds. Angiogenesis was observed in core regions of crosslinked scaffolds, but not uncrosslinked scaffolds. Conjugation of chondroitin sulfate to the collagen scaffolds in combination with crosslinking improved both the cellular infiltration and angiogenesis compared to uncrosslinked and crosslinked scaffolds. Correlations between histology and MRI analyses showed that statistically significant relationships existed between cellular density, void area, T_2 and apparent diffusion coefficient (ADC) measurements demonstrating that MRI is sensitive to specific remodeling parameters. Understanding the relationship between histology and MRI parameters may be used to help guide the interpretation of MRI data as well as to reliably detect changes within the implants using the MRI data alone, reducing the need for scaffold harvesting and destructive testing.

Table of Contents

Table of Tables

Table of Figures

Acknowledgements

I would like to thank my advisor *George Pins* for his unwavering support during my time at WPI. His patience and guidance are greatly appreciated.

Christopher Sotak, co-advisor for this project and my committee member, has provided valuable scientific insight and direction that has helped steer this project.

Glenn Gaudette I would like to thank for his interest and assistance in completing this project and serving on my committee.

My good friend *Sivakumar Kandasamy* for never refusing to help and his consistent maturity and perspective throughout the project.

Joseph Labenski, who helped with my data collection and processing.

My laboratory mates, *Katie Bush* and *Kevin Cornwell*, for their support and help troubleshooting experiments as well as their numerous suggestions.

Jacques Guyette for his assistance with staining.

My *family* for their understanding, support and much needed breaks.

1 Introduction

Medical technology to repair or replace damaged tissues has been greatly influenced by the emergence of tissue engineering and regenerative medicine. Implants that enhance the healing process, by providing a provisional cell scaffold have become a significant focus of biomedical research and an active area of research.

The continued improvement of implantable tissue engineering devices depends on the ability to collect relevant data to assess the performance of the implant. During the development of implants, researchers and clinicians must evaluate the functionality of the implant and the surrounding tissue response. Current data collection methods to evaluate critical parameters of implant performance are commonly limited by invasive techniques, such as histological analyses of explants. These destructive, end-point analyses limit the rate that data can be obtained from samples and increase the degree of statistical error associated with sample to sample variability in time course studies.

Magnetic Resonance Imaging (MRI) has become an indispensable diagnostic tool in the clinical setting for characterizing pathologies, such as stroke[1] and tumors,[2] due to its sensitivity to changes in water content and the particular water environment. This tool is used to monitor soft tissues by measuring vascularity, cellularity and water diffusion. We hypothesize that MRI can be used as an enabling technology to monitor and assess implants and to facilitate high-throughput analysis of tissue engineered devices, by noninvasively providing the same information as histological techniques. This would provide researchers the ability to study implants without having to destroy them.

Collagen is a widely used implant biomaterial used in many tissue engineering devices. Artificial skin equivalents[3, 4] vascular grafts,[5] meniscus repairs,[6] drug

delivery devices[7] are all research areas where the possibility of using collagen is being explored, or where actual collagen-based devices are available on the market and in clinical use. The highly conserved structure of collagen across species, which gives rise to its inherent biocompatibility, as well as its tolerance for certain manufacturing techniques, makes collagen a widely used biomaterial and a natural choice for this study.

The current methods for evaluating implants, in the majority of cases reported in the literature, rely on predefined, semi-quantitative scales. Blinded pathologists score tissue sections using a pre-defined scale for parameters that are relevant to the particular study. This usually includes parameters such as the relative numbers of cells and their type, the foreign body reaction, angiogenesis within the implant and area of affected tissue surrounding the implant. These measurements provide an easy metric to compare the relative differences in tissue response between types of implants but are difficult to correlate with MRI measurements because the scale is usually arbitrary. For this study quantitative histological techniques were developed to avoid the use of pre-defined scales.

In this study, scaffolds with varied and predictable responses were implanted subcutaneously in rats and evaluated using quantitative histological techniques to characterize the tissue response. Concurrently, implants were imaged using MRI to observe changes in these data with increasing implantation time. Histological measurements were correlated with MRI data to determine which parameters provide the best assessment of the implant in terms of degradation, cellular density and angiogenesis.

A wide range of tissue responses were observed by measuring changes in cellular density, blood vessel density and void areas based on differences in crosslinking

treatment. Statistically significant correlations between the histology and MRI data were found, showing that MRI can indeed be used to monitor changes within the collagen scaffolds.

The correlation data will be used to help guide the interpretation of future MRI data so that studies may be able to reliably detect changes within the implants using the MRI data alone, reducing the need for scaffold harvesting. Understanding the relationship between histology and MRI parameters will eventually allow for the monitoring of implants in a clinical setting, preventing unnecessary surgical revisions or alerting clinicians that a change in treatment is required before complete failure of the implant.

2 Background

The development of a noninvasive technique to monitor collagen scaffold implants requires an understanding of the implants, their interactions with the surrounding tissue, and the proposed imaging modalities. Selected methods to form the initial shape and structure of the implant as well as the methods used to biochemically tailor the implant for specific applications are reviewed to provide an understanding of the nature of the implant. The biological responses to implantation and the methods used to evaluate the implants are also discussed. Finally, the fundamental physics of MRI that give rise to the various parameters is briefly presented to provide an understanding of the underlying principles. Previous MRI studies to evaluate implants and their results are also presented.

2.1 Collagen Matrix Fabrication

Collagen is well documented as a biomaterial for medical applications. Collagen implants are used for medical devices for applications including drug delivery, wound dressings, tissue and bone fillings, dental repair, and vascular defects.[8,9,7,10,11] Part of collagen's wide applicability is due to the many forms that collagen can be crafted into and its excellent biocompatibility. As a major component of the extracellular matrix (ECM) in higher mammals, cells recognize and respond to the biochemical surface features of collagen in a manner that closely emulates a native wound healing response. Furthermore, these biochemical features can be modified to suit the specific application either by incorporating biologically active molecules or by chemically modifying the implant. The material is easily remodeled and integrated into the surrounding tissue via native enzymatic pathways, followed by new collagen synthesis by the host. Collagen

scaffolds are of particular interest because of their suitability as cell-based scaffolds.[12] In addition to the biochemical benefits of collagen, the physical structure of scaffolds can be controlled to suit particular applications. The high void volume and interconnected pore structure provide space for cellular infiltration and transport of nutrients and waste through the scaffold.[9] For example, to create functional dermal analogs, scaffolds must be fabricated with average pores sizes between 20 and 125 μm.[13] Additionally, collagen is readily available from many natural sources.

2.1.1 Lyophilization

Many techniques have been developed to control the size of the pores and to achieve the inter-connected pore structure necessary for cellular infiltration and mass transport within implantable scaffolds. These include solvent-casting, particulate-leaching, gas foaming, phase separation, fiber meshes/fiber bonding, melt molding and freeze drying.[14] However, with the exception of gas foaming and freeze drying, these techniques require harsh organic solvents that limit their use to the fabrication of synthetic materials. These techniques also create closed or dead-end pores rather than the desired interconnected pore structure. Collagen scaffolds are most commonly prepared using a freeze drying, or lyophilization, process.

Freeze drying is performed by freezing a dispersion of insoluble collagen prepared in a weakly acidic solution. The formation of ice crystals forces collagen to localize between the crystals creating an interpenetrating network of collagen and ice crystals. The ice is then sublimated, leaving behind a pore structure that mirrors the ice formation.[15] Controlling the freezing conditions allows the pore organization to be precisely controlled.[15,16] During the freezing process the thermal gradients within the

scaffolds lead to distinct freezing lines, particularly on the side of the scaffold not exposed to the atmosphere, sometimes referred to as the "pan-side." These freezing lines are oriented by the thermal gradient. The situation is further complicated by changes in thermal gradients as the temperature of the dispersion changes. These cause changes in the orientation of the freezing lines and also contribute to the heterogeneity in the scaffold.

An additional source of scaffold heterogeneity is the creation of a morphologically distinct "skin" layer at the surface of the sponge exposed to the surrounding atmosphere. This layer develops due to greater solvent evaporation at the dispersion-air interface than within the dispersion.[17] The greater concentration of collagen at the surface creates pore sizes that are generally smaller compared to pores found deeper in the sponge. This layer of different pore sizes effects mass transport through the sponge as well as cellular attachment and infiltration.[15] Careful attention will need to be given to these processes to ensure the sponges are created with biologically functional pore sizes. For these studies, the scaffolds should be as homogenous as possible to simplify the analyses.

2.1.2 Crosslinking

In addition to manipulating the physical structure of sponges, chemical techniques have been developed to enhance the degradation rate and the biofunctionality of sponges to further tailor them to specific applications through biochemical modifications.

The particular environment into which the sponge will be implanted can vary greatly. For example, in a burn wound where a collagen sponge would be used as a skin graft, there are high concentrations of proteolytic enzymes.[18] These enzymes degrade

the sponge faster than if the sponge is placed in a bony defect to guide osteoblast activity. It is often the case that the collagen is degraded faster than would be desired for optimal healing due to the fact that collagen is prevalent in the body and therefore susceptible to a large number of enzymes that efficiently degrade foreign material. Various techniques have been developed to modify collagen sponges so that their resistance to degradation is appropriate for the particular implant environment or application. The most common method for increasing the degradation resistance of scaffolds is to introduce additional chemical bonds between the collagen molecules, termed crosslinks. Similarly, the tensile strength of the sponge and other mechanical properties can be increased by crosslinking. Crosslinking also believed to reduce the immunogenicity of the collagen by masking certain antigens, allowing for xenogenic collagen to be implanted without causing a chronic immune response.[19] These bonds can be formed using physical or chemical strategies. Physical methods do not introduce exogenous chemicals that may remain within the scaffold and detrimentally influence the biological response post-implantation. However, the degree of crosslinking can be challenging to control, and other effects, such as changes in wettability, are often deleterious. Chemical crosslinking provides a greater control and residual chemicals can be removed by diligent rinsing after the cross-linking.

Chemical crosslinking methods usually involve the use a bifunctional chemical agent that reacts with two collagen molecules, at two different sites, to create a bond between them by becoming incorporated into the chemical linkage. Ideally the bonds formed should be irreversible and stable. The chemicals that have been used previously to create crosslinks are glutaraldehyde, formaldehyde, polyepoxy compounds, acyl azide, carbodiimides, hexamethylene diisocyanate and chromium tanning.[7,20] Exceptions to

the bifunctional nature of most crosslinkers are carbodiimides, which only facilitate the formation of bonds without actually becoming part of the linkage.[7] Only carbodiimides are discussed in detail here as this is the primary method employed for these studies. For a complete review of collagen crosslinking see Friess[7] and Khor.[20]

2.1.2.1 Carbodiimides

The principle advantage of using carbodiimides is the molecules are not required to be bifunctional and highly reactive to create the stabilizing bonds.[7] This results in more predictable reactions and fewer unwanted, side reactions. The most common chemical used in the class of carbodiimides to crosslink collagen is 1-ethyl-3-(3-dimethylaminopropyl) carbodiimide hydrochloride (EDC). EDC is widely used to conjugate proteins in many biotechnology processes.[21] The molecule activates the carboxylic acid side groups of proteins, usually aspartic and glutamic acid residues in the case of collagen, which then react with the amine groups of other polypeptide chains to create amide bonds.[22] The mechanism for this reaction is shown in Figure 1.

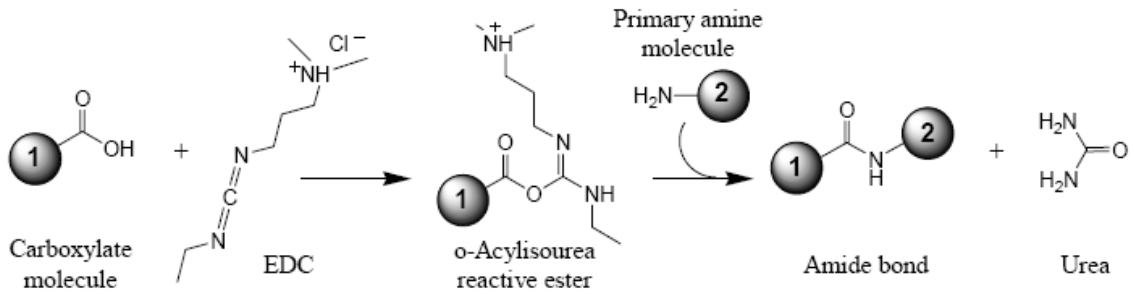

Figure 1: EDC crosslinking mechanism
Adapted from [23]

Crosslinking is performed in a mildly acidic environment to provide excess protons to initiate the reaction. The specific pH of the reaction solution has been shown to effect the type of crosslinking that occurs.[24] Optimization studies have found a pH of 5.0-5.5 to be most effective.[24,25] Due to the unstable amine reactive intermediate shown in Figure 1, the conditions of crosslinking have to be very carefully controlled to minimize unwanted side-products. Specifically, the hydrolysis of the ester bond to produce the original carboxylic group on the protein and the subsequent alcohol substitution on the second imide bond, serve only to deactivate the crosslinker. To prevent this, N-hydroxysuccinimide (NHS) is added to the reaction solution.[25,26] The structure of NHS is shown in Figure 2. This compound is more reactive than water and activates the ester bond before it is hydrolyzed. The activated ester can then react with the amine group on an adjacent collagen molecule to create the crosslink.

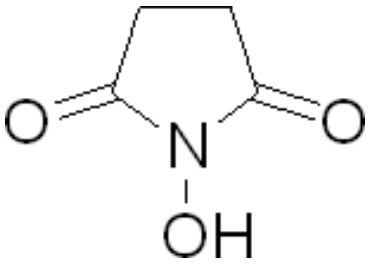

Figure 2: Structure of *n*-hydroxysuccinimide
Adapted from [27]

Comparable crosslinking densities to glutaraldehyde, as measured by shrinkage or denaturation temperature, have been obtained using EDC.[28,25] Increased compressive stiffness for cartilage implants[29] and reduced calcification[30] have also been demonstrated with EDC crosslinking compared to glutaraldehyde treatment.[29] Furthermore, calcification of EDC treated implants is much less than glutaraldehyde implants post implantation.[28,30]

EDC is limited by the number of amine groups available for reaction on the collagen molecule.[31] The repeating tripeptide, Gly-X-Y (where X and Y are most frequently proline and hydroxyproline respectively), which makes up collagen, and the

tightly wound helical structure cause the number of available amine to be approximately 30 groups per 1000 residues.[32] The number of available carboxylic acid groups is greater, at approximately 120 groups per 1000 residues.

A significant advantage of EDC crosslinking over other crosslinking methods is that it can be used in predictable manner to directly conjugate other proteins to the collagen matrix during the crosslinking treatment. Frequently, researchers have attempted to direct cellular activity by incorporating specific ECM molecules into the matrix that cells will recognize. The EDC molecule will react with proteins in solution and covalently bond them to available collagen molecules. This strategy has been used to conjugate glycosaminoglycans (GAGs), which have been shown to influence fibroblast behavior, to the collagen matrix to improve biocompatibility.[33, 34] The mechanism for this is shown in Figure 3. This method could be used to attach a variety of molecules to the collagen matrix such that they are presented in a biological functional conformation,

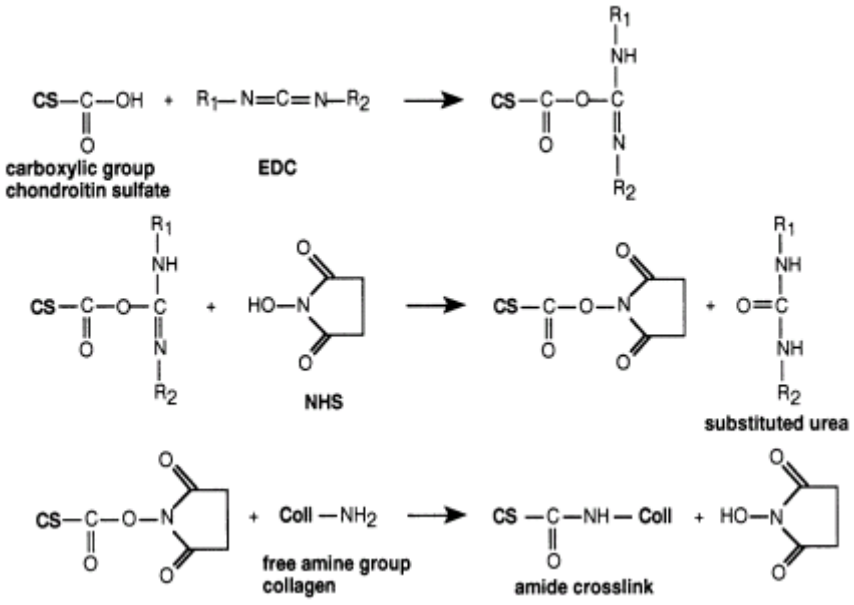

Figure 3: Conjugation of glycosaminoglycan to collagen using EDC
Adapted from [26]

provided they have a carboxylic group that can be modified without changing the bioactivity of the molecule.

In this project, the ability to modify the scaffold to elicit different tissue responses will be utilized to create scaffolds with greatly varied yet predictable responses. Large differences in the responses to the implant will increase the likelihood of discerning these tissue differences with MRI. Previous studies examining the effects of different modifications to collagen matrices on the host responses are described below.

2.1.3 Influence of Glycosaminoglycans

Glycosaminoglycans are a class of ECM components that modulate cellular responses to scaffolds. In physiological environments, glycosaminoglycans are present as side chains attached to larger proteoglycans.[34] The different hexuronic acids and hexosamine molecules link together in disaccharide repeating units with various sulfation patterns to create a wide variety of proteins that precisely direct various cell functions,[35] see Figure 4. Cells attach to these proteins via integrins that initiate a signaling cascade within the cell that influence the cellular behavior.

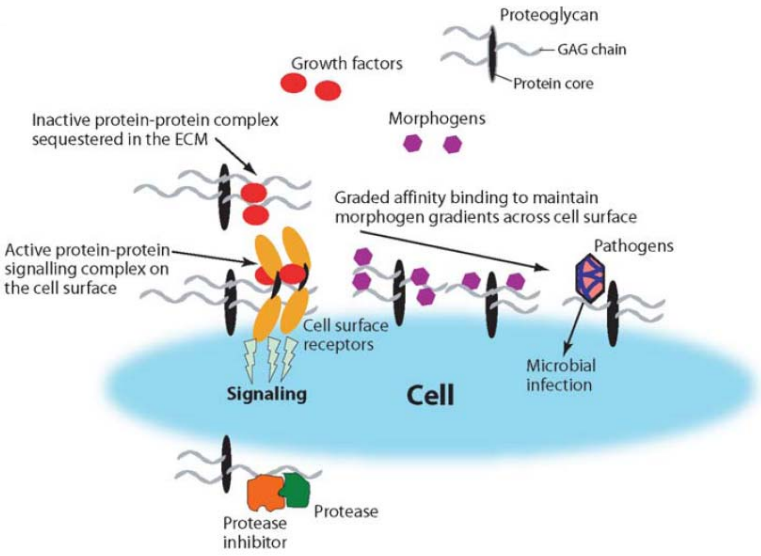

Figure 4: GAG function in ECM
Adapted from Sasisekharan [35]

Commonly studied glycosaminoglycans used in tissue engineering include heparin, heparan sulfate, dermatan sulfate, chondroitin sulfate, hyaluronan and hyaluronic acid.[36] Increased fibroblast migration with the use of hyaluronate and chondroitin sulfate have been reported.[33] Reduced foreign body reactions to collagen matrices with conjugated chondroitin sulfate and heparan sulfate have been demonstrated in subcutaneous implants.[37] The use of collagen-GAG copolymers, which contain chondroitin sulfate, has also been studied extensively for use as skin regeneration templates.[13]

The ability to incorporate glycosaminoglycans into collagen scaffolds can be used to control the cellular behavior both *in vitro* and *in vivo*. This approach will create significant differences in the tissue responses to the implants maximizing the likelihood of detecting these differences using MRI.

2.2 Collagen Matrix Implantation

Preliminary *in vivo* studies of various collagen matrices are most commonly performed using subcutaneous implantations, usually within dorsal compartments of rats. This is due to the ease of surgery for both placing and retrieving the implant. Subcutaneous implantations also facilitate MRI evaluation, as it allows for surface coils to be used instead of volume coils that generally have lower signal to noise ratios.

Previous studies have extensively characterized tissue responses in this implant environment, making it a suitable choice for these studies.[38,39] Tissue responses to implants are challenging to analyze quantitatively due to the complexity of living systems. Depending on the particular interest and aims of the researcher, different parameters may be measured. These include the number and type of cells around and within the implant,

the activity of these cells in terms of protein synthesis and extracellular matrix (ECM) remodeling, as well as changes to the implant itself.

2.2.1 Physiological Outcomes

The numerous parameters that can be measured after the implantation of a medical device make the complete characterization of the tissue response challenging. Certain responses, such as the production of a discrete protein or cellular migration, may be more important to some types of implants. The development of a noninvasive technique to monitor implants should be as general as possible to maximize its utility for various applications. This thesis will concentrate on physiological outcomes that are fundamental to the success of all types of artificial tissue constructs. Biocompatibility, degradation rates and angiogenic potential are all critical design criteria for implants that a noninvasive technique should be able to monitor. These parameters have been extensively explored and consequently are well characterized in the literature.

2.2.1.1 Biocompatibility

The biocompatibility of an implant is a critical factor that must be addressed during the design and development. The initial inflammation caused by the presence of the implant, a foreign material, and surgical implantation, is important to assess. This response has a direct effect on the later tissue response as the wound healing cascade progresses. The type and number of cells that are recruited to the implant environment, as part of the inflammatory response, have been previously studied to determine the biocompatibility of collagen implants.[40,41,42]

Polymorphonuclear cells (i.e. neutrophils) and monocytes/macrophages are the cells most commonly associated with foreign body induced inflammation. Chemotactic

factors released during the inflammation recruit reparative cells, including fibroblasts, to the wound environment.[10] A schematic of the evolution of cells surrounding the implant is shown in Figure 5. These cells are usually identified and counted using a histological stain, such as hemotoxylin and eosin or toluidine blue, where the shape of the nucleus can be used to identify the cell.

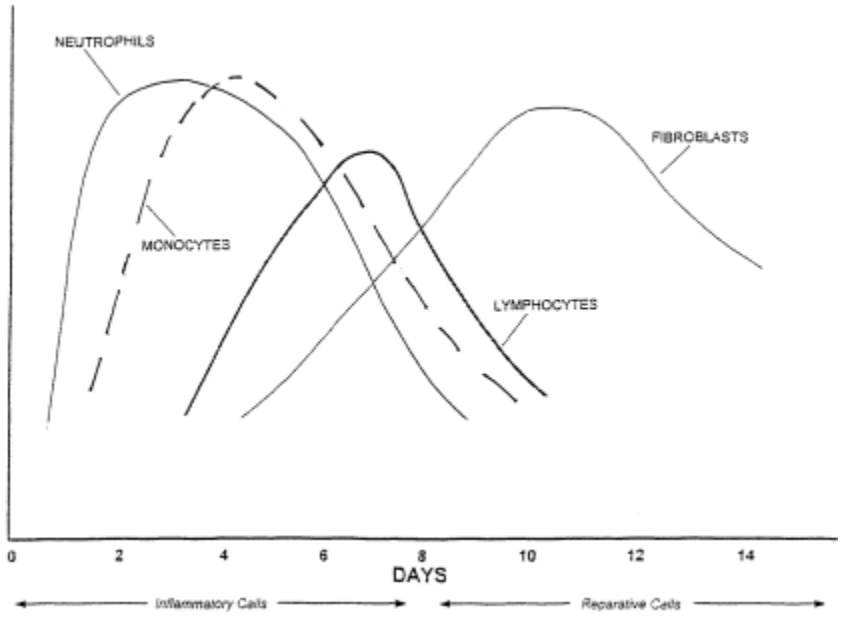

Figure 5: Evolution of cell type surrounding implant
Adapted from [10]

Manual counting of individual cells in histological sections of tissue explants is prohibitively time consuming. Semi-quantitative assessments have been previously reported by scoring randomly selected fields of view (FOV) for the number of cells within in the implant based on an arbitrarily defined scale. These measurements are taken blinded by multiple researchers.

2.2.1.2 Angiogenesis

The ability to support angiogenesis has been identified as a critical factor for the success of tissue engineered scaffolds and consequently has received considerable

attention.[43] Cells cannot survive further than a few hundred micrometers from the nearest capillary. The regeneration of tissues larger than this requires vasculature to support viable cell populations within the scaffold. Angiogenesis can be measured by quantifying the number of vessels within the implant using a variety of methods. Staining for markers specific to the microvasculature in explants allows capillaries to be identified. Antibodies directed against the basal lamina marker collagen IV, platelet endothelial cell adhesion molecule-1 (CD31 or PECAM-1) and von Willebrand factor have all been used previously.[44] Perfusion measurements using microangiography[45], computed tomography[46] and magnetic resonance micro-angiography[47] have been described to measure blood flow *in vivo*. Alternatively MRI data that could correlate with the histological staining data, are *in vivo* measurements with gadolinium-based contrast agents such as gadopentate, gadoteridol and gadodiamide that are used to measure the perfusion of blood in a specific region of interest.[48]

2.2.1.3 Degradation

Tissue scaffolds are designed as temporary constructs that are slowly degraded and replaced by native tissue. The scaffold should persist long enough to facilitate new tissue ingrowth and wound healing, but should not persist and impede remodeling and neotissue regeneration. The rate of biodegradation must be carefully controlled to achieve optimal wound healing.[13]

The degradation extent of collagen scaffolds can be measured using a variety of methods. *In vitro* studies have previously used the change in dry mass[22], or spectroscopic methods, such as the hydroxyproline assay[49] to determine the concentration of solubilized collagen. Mechanical properties have also been used to

determine the integrity of the scaffold. Changes in tensile strength[22], compressive modulus[50] and stress relaxation[51] have all been previously reported.

In vivo studies have described histomorphometry techniques to measure the extent of degradation.[52] This is performed by measuring the area of each of the different regions on a slide, such as regions occupied by the implant material versus new tissue, blood vessels or empty space. As the matrix degrades, the area it occupies in a randomly chosen FOV should decrease. This analysis is usually carried out with the aid of a computer. Excised collagen matrices have also undergone mechanical tests to assess the degradation.[53] Alternatively, fluorescently-labeled antibodies targeted against the particular collagen species that the implant is made from can be used to quantify the amount of fluorescence and persistence of an implant. However, histomorphometry provides quantitative data in an easier, more efficient manner than fluorescent imaging of tissue sections.

2.2.2 Responses to Matrices

The development of a noninvasive technique to monitor implants requires model implants with predictable and varied ranges of tissue responses for detecting a difference using MRI. It will also allow a large range of data histological data to be correlated with the MRI measurements. The different responses to collagen matrices are based on the different fabrication treatments they undergo prior to implantation. This section will briefly review how the different treatments affect the biological response.

Crosslinking has a significant effect on the tissue response to collagen matrices. Glutaraldehyde crosslinking has been shown to produce a greater initial inflammatory response compared to EDC crosslinking[28] and diisocyanate.[28,40] However, cellular

infiltration of fibroblasts towards the center of the sponge at longer time periods was shown to be decreased as a result of glutaraldehyde crosslinking. Cellular infiltration and inflammatory response is greatest in uncrosslinked sponges.[54] Furthermore, increasing the glutaraldehyde crosslinking times were shown to decrease the initial inflammatory response.[54] This is caused by the masking of antigens by crosslinks.[55] EDC crosslinking produces samples with equivalent resistance to proteolytic attack, while improving the biocompatibility and amount of tissue ingrowth over glutaraldehyde treated samples. The degradation rates for these crosslinking techniques were all found to be slower than uncrosslinked sponges.

The incorporation of glycosaminoglycans (GAGs) and growth factors is another frequently used method to improve the tissue response.[41,42,37,13,56] In a study performed by Pieper *et al*.[37] the addition of heparan sulfate and chondroitin sulfate was found to reduce the transient inflammatory response, increase infiltration by fibroblasts and increase the rate of new tissue deposition over uncrosslinked sponges and sponges crosslinked without GAGs.[37] The results from this study are summarize in Table 1 . The presence of GAGs also decreased the degradation rate, preserving the porous structure compared to sponges with the same crosslinking density. The sustained release of basic fibroblast growth factor has also been shown to increase new production and increased angiogenesis.[57]

Table 1: Tissue response to glycosaminoglycans

Cellular Events	UnX	EDC	EDC+CS	EDC+HS
Inflammatory/immune cells	++	+++	+	++
Fibroblasts/ECM deposition	++	+++	+++	+++
Angiogenesis	+	+	++	+++

UnX = uncrosslinked, EDC = crosslinked using EDC carbodiimide, EDC+CS = EDC crosslinked with chondroitin sulfate, EDC+HS = EDC crosslinked with heparan sulfate. Cellular events were scored as slight (+), moderate (++), and abundant (+++) Table adapted from Pieper *et al.* [37]

2.3 MRI Overview

Magnetic resonance imaging has emerged as a powerful tool in a variety of medical applications. Its sensitivity to small changes in water environments and ability to probe tissues noninvasively has enabled it to become an extensively used technique. The basic physical principles that give rise to a nuclear magnetic resonance (NMR) signal and how this is used to create an image are briefly explained here. The basic types of images will also be discussed. This section, adapted from Smith[58] and Haacke[59] describes the principles governing MRI to provide a basic, working knowledge of the technique as it applies to this project. The reader is referred to other texts for a more thorough treatment of this material.

2.3.1 Nuclear spin in a Magnetic Field

Atoms with an uneven of number of neutrons or protons have a nucleus with a magnetic dipole arising from the unpaired spins of the nuclear particles. A nucleus with a magnetic dipole can be considered analogous to a miniature bar magnet, with north and south poles, commonly represented as a vector. These nuclei will interact with an external magnetic field, and are termed NMR active nuclei. Commonly occurring NMR active isotopes include ^{1}H, ^{14}N, ^{23}Na, and ^{31}P. The high abundance of ^{1}H, simply a

proton, makes it a common atom to use for MR imaging, though it is possible to use other nuclei.[58]

When protons are placed within a large external magnetic field, the interaction between the external field and the nuclear magnetic fields causes the protons to align with the applied field. When the protons are not aligned with the field (as during an experiment, when they have been excited), the interactions between the nuclear spin and the external magnetic field, lead to each proton precessing about the direction of the field. The angular frequency of this precession (ω_0) is given by:

$$\omega_0 = \gamma B_0 \qquad (1)$$

Equation 1: Lamor equation

where γ is the gyromagnetic ratio, a unique constant for each nuclei, and B_0 is the external magnetic field. This precessional frequency is called the Lamor or resonance frequency. For a proton, γ has a value of approximately 2.68 x 10^8 rad/s/Tesla. The precessional frequency of a proton in a typical; magnetic field used in imaging is roughly within the frequency range used for radio waves.

When a large number of protons are placed within a field, as occurs when a patient or specimen is inserted into the bore of a magnet, the protons align in the direction of the external magnetic field, by convention denoted as the z-direction. Only two alignments are possible, parallel or anti-parallel to the magnetic field. The parallel alignment has a slightly lower energy than the anti-parallel state, resulting in a greater number of nuclei in the lower energy state at equilibrium. Most of the individual dipoles in one state will cancel with a proton dipole in the alternate energy state, but the slight excess of protons in the lower energy state will result in a very small net magnetization

aligned along the z-axis. This quantity is called the spin excess and is used to generate the signal detected during NMR data collection.

2.3.2 MRI Parameters and Their Physical Origins

The basic NMR experiment to collect data involves perturbing a system subjected to a magnetic field from its equilibrium state by applying energy to the system. As the system returns to equilibrium, the state of the system is measured as a function of time, by sampling at certain time points. This is a broad simplification but serves illustrate the idea.

At equilibrium, each proton has aligned with the magnetic field and the net magnetization (M_0) is all in the z-direction represented by the symbol M_z ($M_z = M_0$). There is no magnetization in the plane perpendicular to the magnetic field ($M_{xy} = 0$) at equilibrium, also called the transverse plane. A radiofrequency (RF) coil is used to apply energy to the system and perturb it from equilibrium. This is achieved by sending a current through the coil at a frequency that matches the precession frequency of the proton, hence creating resonance and achieving an efficient transfer of energy into the system. By controlling the duration of the current, the net magnetization of the sample can by rotated a specified angle away from the direction of the field. The hardware requirements for the coil, in order to match the frequencies and to achieve uniform excitation of the sample, are beyond the scope of this summary. The system is then left to return to equilibrium. During the restorative period, the same RF coil that was used to initially excite the system detects a current that is induced by the transverse magnetization as it returns to equilibrium.

The following sections will briefly describe the particular quantities that can be measured during an imaging session. This will provide the reader with an introduction sufficient to understand the data that will be presented in this thesis.

2.3.2.1 Longitudinal Relaxation

The longitudinal relaxation time is a measure of the time it takes for the protons to return to equilibrium state after the system has been excited by a 90° pulse. That is, a pulse which moves the net magnetization into the transverse plane such that $M_z = 0$ and $M_{xy} = M_0$. The interactions that cause the protons to relax back to their alignment in the z-direction are primarily due to environmental interactions and so longitudinal relaxation is often called spin-lattice relaxation. As soon as the pulse is turned off, the transverse magnetization will begin to decay to zero and the longitudinal magnetization will recover to its equilibrium value. Mathematically, the recovery of the magnetization in the z-direction can be represented by

$$M_z(t) = M_0\left(1 - e^{\frac{-t}{T_1}}\right) \qquad (2)$$

Equation 2: Longitudinal relaxation

where time, t = 0 right as the pulse is turned off and T_1 is the characteristic parameter that determines the rate of recovery of the longitudinal magnetization. The T_1 parameter can be thought of as the time it takes for the longitudinal magnetization to recover to 63% of its initial value.

2.3.2.2 Transverse Relaxation

In addition to the longitudinal relaxation, there is a faster relaxation process that occurs in the transverse plane. This is sometimes referred to as in-plane dephasing. Initially, the protons are all aligned (phase coherent) immediately preceding the initial

pulse. After this, the spins tend to "spread out" (diphase) due to variations in the local magnetic field caused by neighboring protons. This leads to differences in the precessional frequencies that accumulate over time and tend to "fan out" the spins, thus reducing the net transverse magnetization which is the sum of all the individual transverse components (vectors of equal magnitude, but opposite directions will sum to zero).[59] This is shown mathematically by Equation 3, where again, t = 0 as the pulse is turned off. The T_2 parameter can be thought of as the time it take for the transverse magnetization to decay to 37% of its original value, and is always less than or equal to the longitudinal relaxation.

$$M_{xy}(t) = M_0 e^{\left(\frac{-t}{T2}\right)} \tag{3}$$

Equation 3: Transverse relaxation

Characteristic plots of the longitudinal and transverse relaxation processes are shown in Figure 6, where the T_1 time is 400ms, and Figure 7, where the T_2 relaxation time is 100ms. The magnitudes of M_z and M_{xy} have been normalized.

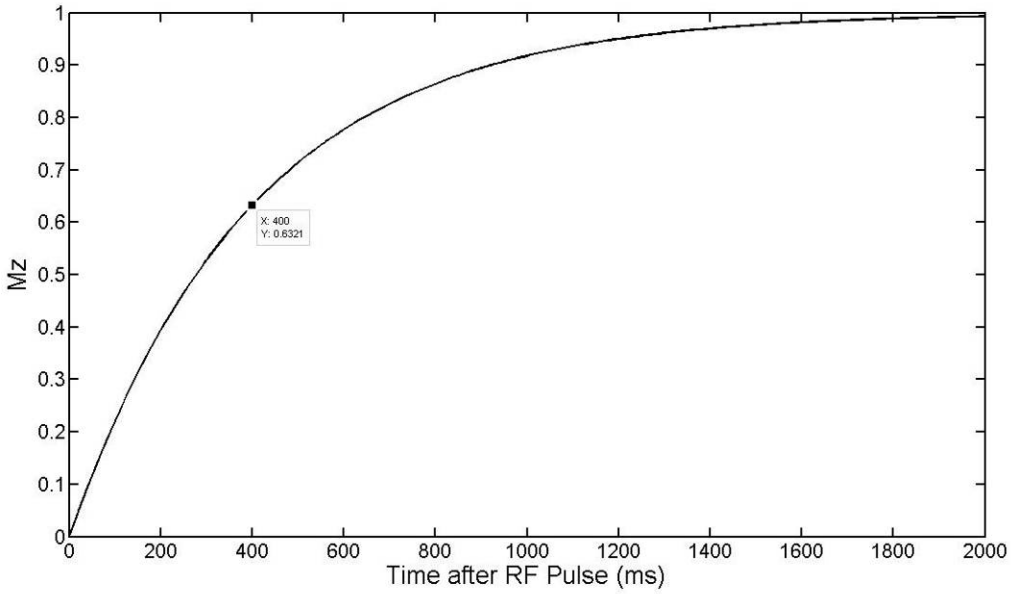

Figure 6: Longitudinal relaxation curve

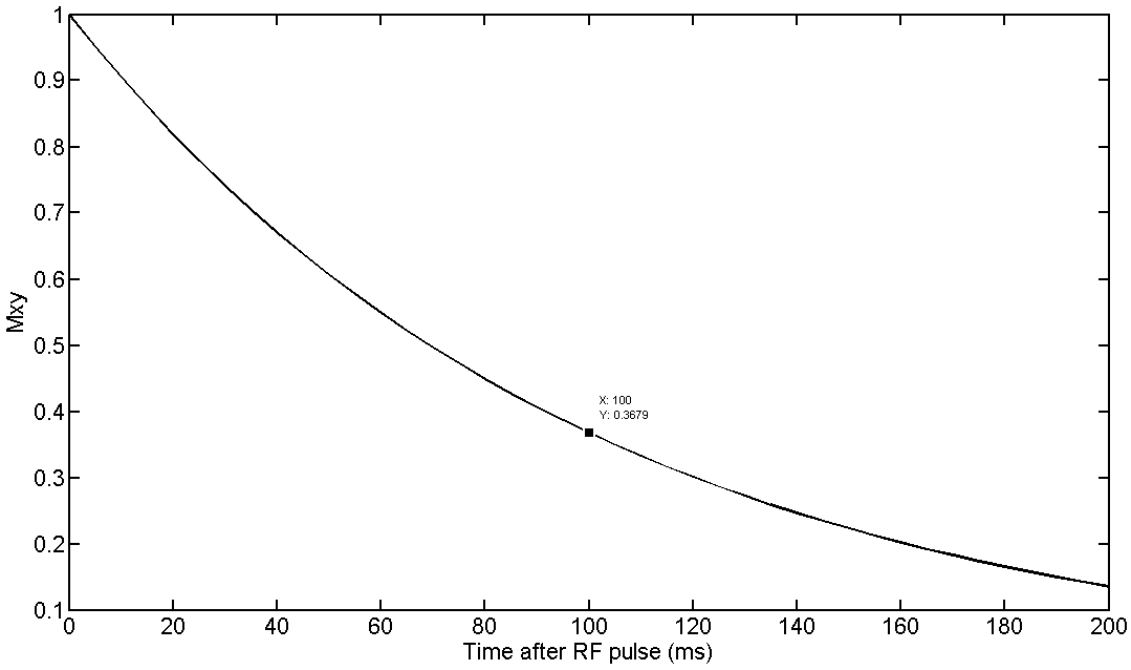

Figure 7: Transverse relaxation curve

2.3.2.3 Image Acquisition

Images require that the electrical signals from protons at different locations within the specimen can somehow be mapped back to their locations when the image is reconstructed. Each pixel within a picture has its location defined by a set of coordinates, usually (x, y), that specify a location in perpendicular directions. In order for the data, essentially induced currents within the RF coil, to be mapped back to the location within the specimen that they originated from, magnetic field gradients superimposed on the external magnetic field encode the spatial position of each volume element into the frequency and phase of the signal. Additional coils within the magnet apply a gradient to the magnetic field that serve to alter the frequency that the protons precess, based on Equation 1. Additional gradients are applied for a short time in the perpendicular

direction to alter the phase of all the protons. The third spatial dimension is controlled during the excitation, where the system is perturbed from equilibrium only in the slice of interest. This is accomplished by matching the frequency of the current in the RF coil with the spins in the slice of interest. Thus, when the data is collected, it can be resolved back to unique (x,y) coordinates (within a specific slice) in an image based on the frequency and phase of the data. The Fourier transformation is used to process the signal collected in the RF coil and to separate it into its individual components.

2.3.2.4 Image Weighting

The two relaxation processes, longitudinal and transverse relaxation, occur simultaneously. When collecting data, it is impossible to halt one type of relaxation, and only measure the other. Thus, when data is collected, there is always a mixture of signals from the two processes. Based on when the samples are taken, and the original pulse sequences used to excite the sample, the data can be collected in such a way that the contrast of the image is dominated by a single relaxation process. This is termed image weighting. Additionally, it is possible to collect diffusion weighted images. This will be discussed in Section 2.3.2.5.

There are two basic timings of the pulses that can be manipulated to achieve the desired image weighting:

- TR interval (time between excitation pulse repetitions)
- TE interval (time at which the signal is measured after the pulse, echo time)

A T_1 weighted image is acquired using a short TR and short TE, which serve to enhance T_1 contrast and minimize T_2 contrast. T_2-weighted images are obtained using long TR

and long TE values, which have the opposite effect. A third type of image-weighting can be obtained using long TR and short TE values, which reduces both T_1 and T_2 contrast and gives a proton-density-weighted image. This is useful in determining how much water is in the specimen.

2.3.2.5 Diffusion Measurements

Collection of MRI data usually employs constant field gradients to spatially resolve the data and to select the various slices of interest. Pulsed-field gradients may be used to encode the data with molecular diffusion information. When molecules move from one region to another, they experience different magnetic field strengths that change their precessional frequencies. These changes in resonant frequencies lead to accumulation of phase shifts (both positive and negative) that serves to attenuate the overall signal. Stationary molecules will not experience the accumulation of phase shifts and exhibit no signal attenuation. Using this data it is possible to create diffusion-weighted images (DWI) that show where there is greater movement of water molecules based on a reduction of the signal.

Pulsed-field gradients can only be used to detect diffusion in the direction of the pulsed-gradient field. Multiple sets of data, with different directional orientations of the pulsed-field gradient, can be combined to obtain an overall description of diffusion in all directions. This is performed to create a map of the apparent diffusion coefficient (ADC). This gives the researcher an idea of how freely the water molecules are moving. While there may be diffusion of other larger molecules, such as proteins, these are generally too slow to be detected using pulsed-gradient fields.

2.3.2.6 Contrast Enhanced Imaging

The mechanisms through which protons transfer energy to their surroundings and thereby relax can be manipulated to significantly alter the relaxation times. The exact principles by which this occurs are beyond the scope of this summary. Alterations to the relaxation times are achieved through the use of MRI contrast agents. These substances, when introduced at low, non-toxic concentrations, interact with the water molecules to accelerate the relaxation processes. The transfer of energy from the spins into the lattice is made more efficient. Image contrast is thereby increased, allowing for better image analysis in certain cases by allowing different tissues to be more clearly distinguished. The change in relaxation times can also be used to monitor the progression of the contrast agent through the tissue. For example, if the agent is introduced intravenously, the blood vessels will experience the change in relaxation times first. As it diffuses out the blood vessels into the surrounding cells, tissues with a greater vessel density will show on the image before tissues with a lesser blood supply. The clearance of the contrast agent can also be used in a similar manner to characterize the tissues.

2.3.3 MRI Implant Evaluation

Previous studies have used MRI to investigate the changes in various biomaterials after implantation. Constantinidis *et al.*[60] used MRI methodologies to monitor cellular distribution and metabolism of adult porcine islet cells and βTC3 cells encapsulated within alginate/poly-L-lysine/alginate beads both *in vitro* and *in vivo*. They showed that diffusion-weighted imaging is most useful for locating the spheres within mice and that the metabolism of the cells can be monitored using NMR spectroscopy.

It has also been shown that changes in T_2 relaxation times are sensitive to changes in the histological state of the poly[N-(2-hydroxypropyl) methacrylamide] (PHPMA) (a hydrogel) implants. In this study, Traoré *et al.*[61] found that the T_2 relaxation data could be fitted using a biexponential model after a certain amount of time within the animal, indicating heterogeneity within the implant. This could be attributed to cellular infiltration creating distinct volumes within the implant, that could be distinguished using MRI, where slow and fast T_2 relaxation times were associated with volumes containing few cells or many cells, respectively. Other studies using NMR imaging and spectroscopy, as well as cell labeling, have characterized implants and tissue responses.[62,63,64] Choi *et al.*[64] have used gadolinium-enhanced magnetic resonance imaging to study the fibrovascular ingrowth into polyethylene orbital implants. They found that the area of fibrovascular tissue, as measured by histology and MRI, correlated very well.

MRI is also extensively used in the clinical setting to evaluate the pathology of soft tissues. T_2-weighted imaging has been used in stroke[65] and tumors of various organs such as the heart,[66] pancreas,[67] and liver[68]. T_1-weighted imaging is generally most useful to obtain information about the general anatomy as it provides good structural images of the various organs. Diffusion-weighted imaging is often used in assessing multiple sclerosis[69] and in the imaging to tumors.[70-72] The relationship between cellular density and MRI measurements of T_2 and ADC has been studied extensively in tumors.[70,73,74] These studies have demonstrated that cellularity can be monitored using these parameters. Contrast-enhanced imaging is also used extensively to

assess the vasculature of certain regions and to measure the angiogenesis of tumors.[75] This same approach can be used to measure the angiogenesis within the scaffolds.

These studies, and many others, have examined the affects that physiological changes, which occur in disease states, have on the MRI measurements. They demonstrate significant progress towards understanding how to collect and interpret the MRI data to obtain useful information that can guide clinical diagnoses and treatments. This body of work describes one of the first studies that applies these techniques to assessing tissue responses to implanted collagen scaffolds. An MRI assessment of collagen scaffolds was closely correlated with histological findings to demonstrate that MRI can be used to monitor these implants using techniques similar to those in common use.

3 Hypothesis and Specific Aims

We hypothesized that changes in tissue responses to implanted collagen scaffolds will correlate with changes in the MR images. Specifically, quantitative analyses of cellular infiltration, tissue ingrowth, and vascularization of scaffolds will correlate with MRI measurements of T_2 relaxation times, water apparent diffusion coefficients, and contrast agent uptake/clearance profiles within the implant. The following correlations were tested:

- Average T_2 values and average cellular density
- Average T_2 values and average void area
- Average ADC values and average cellular density
- Average ADC values and average void area

Specific Aim 1: Characterize *in vitro* scaffold degradation.

Scaffolds were fabricated and modified to produce three different groups; uncrosslinked, crosslinked, and crosslinked in the presence of chondroitin sulphate to conjugate this glycosaminoglycan to collagen. To measure the degradation rates, these scaffolds were treated with bacterial collagenase and the collagen degradation products were analyzed using a hydroxyproline assay.

Specific Aim 2: Quantify cellular infiltration into the scaffold.

Scaffolds were implanted into dorsal subcutaneous pockets of rats, harvested at 2, 7, 14, 21, 28, 35 and 42 days, and histological sections were stained using Haematoxylin and Eosin as well as Masson's Trichrome. Cellular density as a function of depth within the scaffold was measured using automated image analysis software.

Specific Aim 3: Quantify vascularization of the scaffold.

Using histological sections obtained from the explants described above, blood vessels within the scaffold were characterized using Masson's Trichrome stained sections to determine the vessel density as a function of depth within the scaffold.

Specific Aim 4: Quantify new tissue deposition within the scaffold.

Using histological sections obtained from the explants described above, the void area remaining within the scaffolds were measured using Masson's Trichrome stained sections, again as a function of depth within the scaffold.

Specific Aim 5: Correlate histology and MRI data.

MRI parameters were correlated with histological measurements of the same scaffold to determine whether correlations were statistically significant and to formulate specific algorithms or criteria that facilitate the interpretation of MRI measurements.

4 Materials and Methods

This section contains a description of the procedures used to accomplish the body of work in this thesis. All chemicals were obtained from Sigma Chemical Co, St. Louis, MO, unless otherwise specified. Details of the MR imaging were summarized from Kandasamy.[76]

4.1 Scaffold Fabrication

Collagen scaffolds were fabricated from fibrillar collagen extracted from bovine Achilles tendon (Sigma, St. Louis, MI). A 1.6% (w/v) dispersion of collagen was prepared in 0.5M acetic acid and left overnight at 4°C. The dispersion volume was doubled with cold distilled water (final collagen concentration 0.8 wt%) and blended in a water-cooled homogenizer for 30min at 4°C. The dispersion was then degassed under vacuum and stored at 4°C. Forty milliliters of the dispersion was placed in an aluminum weighing pan (70mm diameter) and frozen at -80°C. Once completely frozen, the pan was placed in a freeze dryer (Virtis Advantage, Virtis, Inc., Gardner, NY), initially set at -45°C, and lyophilized overnight. Punches of the lyophilized collagen sheet were made to produce disks of diameter 1.5 cm and thickness one cm, weighing approximately 20mg. Scaffolds were stored in a sealed desiccator at room temperature until used.

Scaffolds were crosslinked using 1-ethyl-3-(3-dimethyl aminopropyl) carbodiimide (EDC) in the presence and absence of shark cartilage chondroitin 6-sulphate (CS), according to previously described protocols,[37,26] to create differential tissue responses that would be detected by both MRI and histological analyses. Scaffolds were initially hydrated under vacuum in 50mM of 2-morpholinoethane sulphonic acid (MES) prepared in 40% (v/v) ethanol and adjusted using 1N NaOH/HCl to pH = 5.0

(referred to as MES buffer). A crosslinking solution containing 0.4294g EDC and 0.1473g *n*-hydroxysuccinimide (NHS) per gram of collagen scaffold to be crosslinked. Solution volumes and reagent masses were varied depending on how many samples were prepared. To conjugate CS to the scaffolds during the crosslinking process, CS was added to the crosslinking solution to make a 1.2% solution (w/v, chondroitin sulphate to crosslinking solution). Scaffolds were then incubated in the crosslinking solution and crosslinking was allowed to proceed for four hours at room temperature. Scaffolds were then rinsed with 70% (v/v) ethanol (4 x 30 minutes) and sterile phosphate buffered saline (5 x 15 minutes). The scaffolds were left in the final PBS rinse and stored at 4°C for no more than two days. Three types of scaffolds were fabricated: uncrosslinked (UnX), crosslinked (EDC) and crosslinked in the presence of CS (EDC+CS).

4.2 In Vitro Degradation of Scaffolds

Scaffold degradation was investigated using previously described methods for enzyme treatment by Pieper *et al.*[26] and hydroxyproline measurement.[49] Scaffolds were rinsed in 0.1M Tris-HCl buffer containing 0.05M $CaCl_2$ (pH 7.4). A proteolytic solution was prepared by dissolving bacterial collagenase (*Clostridium histolyticum*, Calbiochem, San Diego, CA), at a concentration of 200 collagen digestion units (CDU) per ml, in the same Tris-HCl buffer. All solutions were maintained at 37°C during the degradation and scaffolds were agitated on a gyratory mixer. Samples (1ml) were taken daily, after centrifuging tubes at 2,000 rpm (Allegra 6R, Beckman-Coulter, Fullerton, CA) for five minutes, and replaced with fresh collagenase solution. Each sample was stored frozen at -20°C until analyzed for hydroxyproline content. Photographs were taken using a digital camera (Nikon D50, Nikon Corporation) at each sample time.

Hydroxyproline concentrations in the supernatant samples from degraded scaffolds were assessed according to the method of Woessner.[49] A buffer (H-Pro buffer) was prepared by combining 12 ml glacial acetic acid, 50 g citric acid monohydrate, 120 g sodium acetate trihydrate, 34 g NaOH and bringing to a final volume of one liter (pH 6.0). Half-milliliter portions of the supernatant samples, and standard solutions of known collagen concentrations, were combined with a half-milliliter of 12 N HCl in glass test tubes sealed tightly with Teflon-lined screw caps (Fisher Scientific, Springfield, NJ). The samples were then hydrolyzed at 110°C for 18 hours in an oven. Tubes were then cooled and the hydrolyzates were neutralized with 6 N NaOH containing Phenol Red. Fine adjustments were made to ensure the pH was between 6.0 and 7.0, corresponding to an orange/yellow color of the indicator. Each hydrolyzate was brought to a total volume of seven ml using distilled water. Portions of hydrolyzate (75 µl each) were placed in individual wells of a 96-well plate. Then, 37.5 µl of 0.05 M of chloramine-T (sodium *p*-toluenesulfonchloramide), prepared in H-Pro buffer, water, and methyl cellosolve, mixed in a ratio of 5:2:3, respectively, was added to each well and allowed to react for 20 minutes at room temperature. In the same order that chloramine-T was added, 37.5 µl of 3.15M perchloric acid was added to each well and allowed to react for five minutes at room temperature. In the same order again, 37.5 µl of 1.34 M Ehrlich's reagent solution (*p*-dimethylaminobenzaldehyde dissolved in methyl cellosolve) was added to each well and mixed. After the addition of Ehrlich's reagent, the well plate was heated to 60°C in a water bath for 20 minutes. The plate was then cooled in running tap water for five minutes and the absorbance of each well was read immediately at 561 nm using a SpectraMax 250 spectrophotometer (Molecular Devices, Sunnyvale, CA).

Concentrations were determined by comparing absorbance values against a linear standard curve. When the data were plotted the values were adjusted to account for the dilution due to multiple samples. Two scaffolds of each type were degraded, and thirteen supernatant samples were taken from the collagenase solution of each scaffold during the degradation.

4.3 In Vivo Scaffold Assessment Using MRI

All animals were handled and cared for in accordance with the NIH *Guide for the Care and Use of Laboratory Animals*[77] and all experimental protocols were carried out with the approval of the University of Massachusetts (UMASS) Medical School Institutional Animal Care and Use Committee (IACUC Protocol A-1759). No surgeries were performed at Worcester Polytechnic Institute.

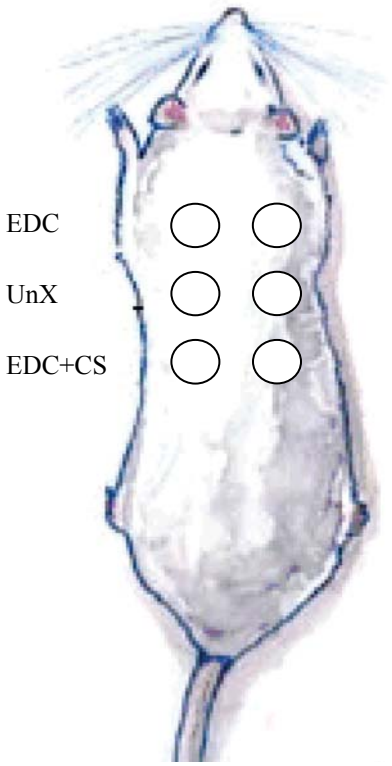

Figure 8: Scaffold implant locations
Adapted from NIH[78]

Male Sprague-Dawley rats (six to seven weeks old, seven rats total) were anesthetized using pentobarbital and xylazine dosed at 40 mg/kg and 10 mg/kg respectively. A dorsal midline incision, approximately six cm long was made from the middle of the thoracic vertebrae towards the tail using a scalpel. Six subcutaneous pockets (three per side lateral to the incision) were made using blunt dissection. A hydrated, sterile-rinsed scaffold was placed in each pocket. The type of scaffold placed at each location is shown in Figure 8. Scaffolds were secured to prevent movement by passing 4-0

monofilament nylon (Ethicon, Summerville, NJ) through the scaffold and skin and tying two knots on opposite sides of the scaffold. Animals were returned to their cages to recover from the anesthesia. Once the animals were ambulant, they were returned to the animal housing facility.

The rats were imaged two days after surgery, and every week after surgery up to six weeks. For imaging, rats were anesthetized by placing them in a closed plastic container and administering 1.5% isoflurane delivered in 1.5 l/min of breathing quality air until the rat was fully sedated. The level of isoflurane was reduced and adjusted as necessary during the course of imaging to maintain sedation. The animal was placed in a custom-built animal holder to control its position within the bore of the magnet and its body temperature was maintained by circulating warm air.

MR imaging was performed using a Bruker Biospin 2.0T/45cm imaging spectrometer and respiratory gating hardware and a custom-built surface coil that allowed all scaffolds to be imaged simultaneously. T_2-weighted images were acquired using a multiple spin echo pulse sequence (TR=2500 ms, TE = 12, 24, 36, 48, 60, 72, 84, 96, 108, 120, 132, 144 ms, Nex = 2). Images were oriented sagittally and each imaging slice was two mm thick.

Contrast-enhanced T_1-weighted MRI was performed using a spin-echo pulse sequence (TR/TE = 600/10 ms, Nex = 2). A pre-contrast image was acquired, and then MAGNEVIST® (Gadolinium-DTPA, Bayer HealthCare) was administered at manufacturer's recommended dosage of 0.1 mmol/kg via a tail-vein injection. Post-injection images were then acquired at regular intervals to monitor the uptake and clearance of the contrast agent.

Diffusion-weighted images were collected using a spin-echo, echo-planar imaging pulse sequence with diffusion sensitization applied along the read gradient at six b-values (b = 15, 60, 140, 390, 560, 760 mm^2s^{-1}). Other acquisition parameters were TR/TE = 2000/53, diffusion gradient duration δ = 4.0 ms, diffusion gradient separation Δ = 35 ms. These data sets were used to created apparent diffusion coefficient (ADC) maps.

Rats were euthanized by intracardiac delivery of euthanasia solution (pentobarbital, 200mg/kg) at days 2, 7, 14, 21, 28, 35, 42. Scaffolds were harvested by cutting the suture that secured it to the skin, taking care to preserve the capsule and surrounding tissue, and excising the scaffold with sufficient peripheral tissue to allow for viewing of normal, unaffected tissue in sections. All scaffolds were then processed for histological analysis. One rat was euthanized at each time point, for a total of 42 scaffold samples.

4.4 Histological Analysis

Scaffolds were placed in tissue cassettes (Fisher Scientific, NJ) and fixed in 10% buffered formalin. After rinsing in tap water, scaffolds were cut along the diameter of the scaffolds as shown in Figure 9. At earlier time points, where the scaffold is much larger, a second cut, perpendicular to the first was sometimes necessary to divide the scaffold into quarters. Photographs show gross morphological appearance of scaffolds at time at removal in Figure 10.

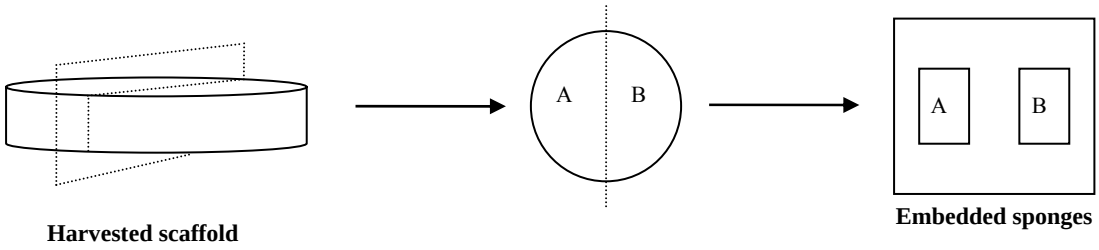

Figure 9: Scaffold processing

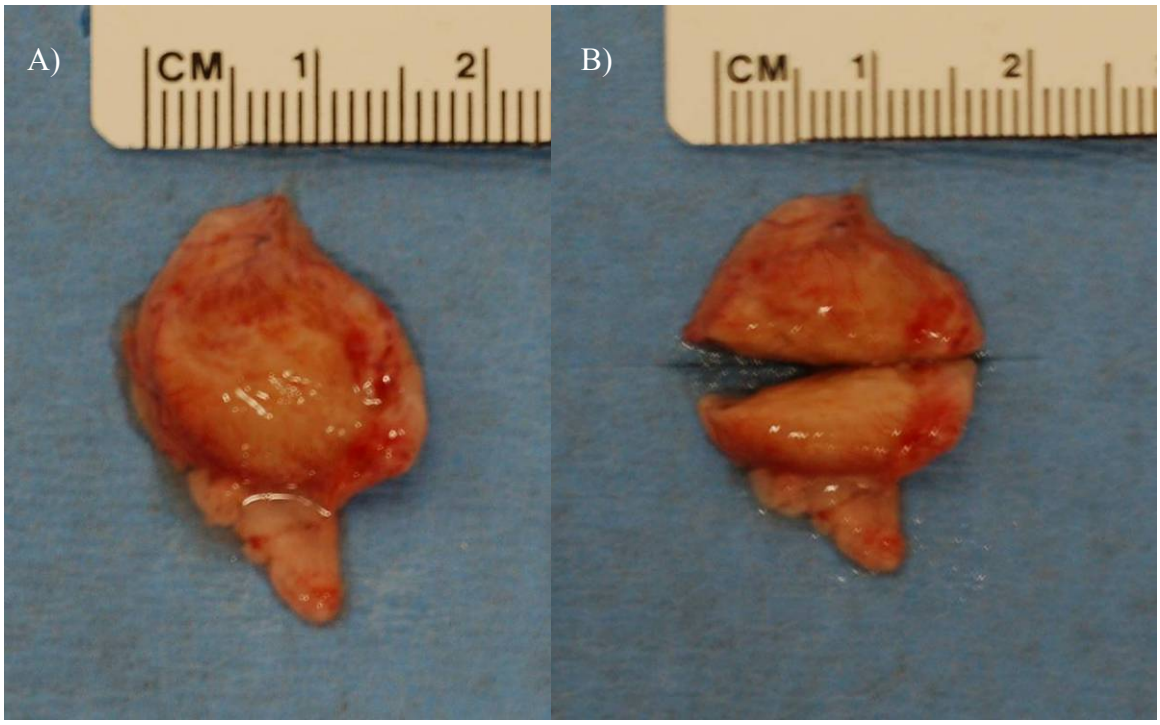

Figure 10: Harvested scaffolds
A) EDC scaffold harvested at 2 days. B) Scaffold cut parallel to midline to facilitate embedding and sectioning.

After fixing and trimming, samples were dehydrated through a series of ethanol baths with gradually increasing ethanol concentrations. Samples were cleared in 2-butanol and embedded in paraffin wax at 60°C such that all the sections were cut in the same plane as the original midline incision made during the implantation surgery. This is the same orientation used to acquire the MR images and allows for easier comparison between MR images and histological sections. Sections were cut at 5 μm on a rotary microtome (American Optical) and placed on poly-l-lysine coated slides (Erie Scientific Company, Portsmouth, NH). Sections were stained with modified Harris Hematoxylin and Eosin (Richard-Allen Scientific, Kalamazoo, MI) and Masson's Trichrome (Sigma, St. Louis, MI) using standard procedures. Slides were mounted with Permount® (Fisher Scientific, NJ) and imaged using a 10x objective on a Nikon E400 microscope, coupled with an RT Color Spot camera (Diagnostic Instruments, Inc Sterling Heights, MI). Image capture was performed using Spot Analysis 4.0.9 software (Diagnostic Instruments). A series of overlapping images were taken across the thickness of the scaffold, from the dorsal to ventral surfaces of the scaffold, including the surrounding fibrous capsule and tissue. Images were then merged into a large, single mosaic using ImageJ (NIH, Bethesda, MD[79]) and the MosaicJ (Swiss Federal Institute of Technology, Lausanne, Switzerland[80]) plug-in.

4.4.1 Thickness

Total thickness of the implant, including the surrounding fibrous capsule, was measured using reconstructed mosaics of the H&E stained sections. Dense, aligned connective tissue was used to identify the capsule.[81] The change from dense connective tissue to looser, normal fascia was used to identify the margin between the capsule and

the surrounding tissue. Within the capsule, the fibrous ribbons of the collagen scaffold were used to identify where the scaffold and capsule met. From these sections scaffold thickness and capsule thickness were measured.

4.4.2 Cellular Density

Cellular density was measured using H&E mosaic images. The contrast between cell nuclei stained blue/black and other structures stained pink/red allowed for easy identification of the nuclei. Each mosaic was divided into 10 equally sized regions (see Figure 11) that spanned the entire thickness of the scaffold and included the capsule, but not the surrounding tissue. As the implant changed size with implantation time, the size of each region changed, effectively normalizing to the thickness of the scaffold. This ensured that an equal number of measurements were taken from each sample and allowed for comparisons between differently sized samples based on relative location within the scaffold. The number of cell nuclei within each region was counted using semi-automated image analysis. A macro was written for ImageJ to facilitate

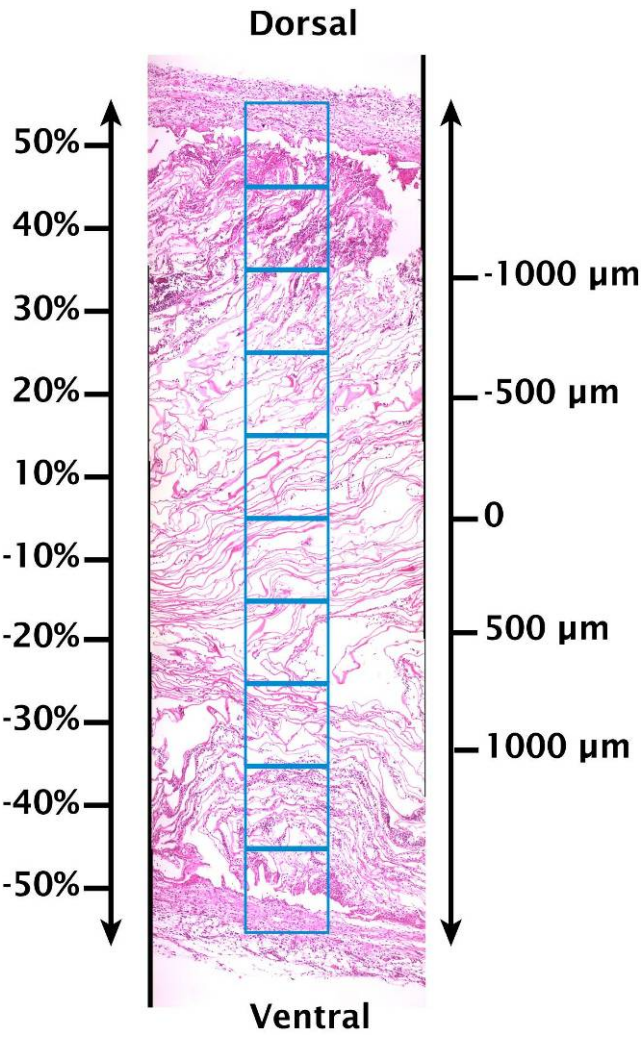

Figure 11: Region selection of an H&E stained cross-section of an explanted scaffold

repeatable, consistent measurements in a time effective manner. A schematic of the approach used in shown in Figure 12. Each image was split into hue, brightness and saturation stacks. The brightness stack provided the best contrast between nuclei and surrounding tissue based on the darker staining of the nuclei. ImageJ commands were then used to subtract background image noise and automatically adjust the contrast and brightness. The resulting image was then converted to a binary image by using the same threshold values for all images to isolate the dark regions (nuclei) of the image. The same threshold values were used in all cases. The "analyze particles" command was then used to automatically count the number of nuclei in the image. For complete details, please see the appendix which shows the code used.

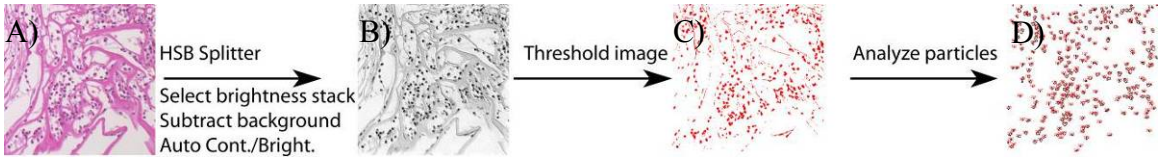

Figure 12: Semi-automated image analysis of H&E stained region to count cells
A ROI of an H&E stained section (A), was split into hue, saturation and brightness stacks. The brightness stack (B) was thresholded (C) and analyze particles were used to count cells (D).

4.4.3 Blood Vessel Density

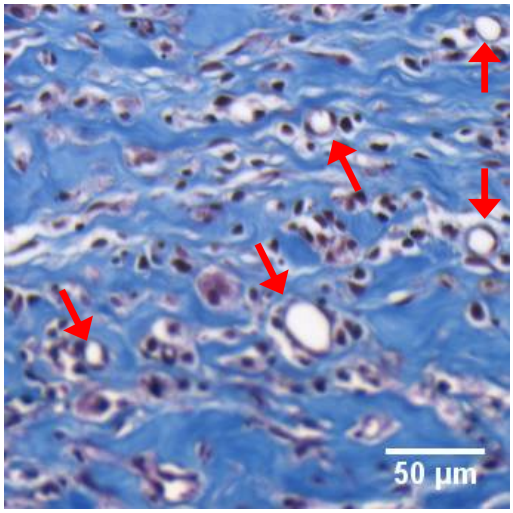

Figure 13: Masson's Trichrome section used to count blood vessels
Arrows show blood vessels.

The number of blood vessels present in each sample was determined using regions taken from Masson's Trichrome-stained sections, using the method described in Section 4.4.2 to divide the scaffold into 10 equally sized regions (Figure 11). Blood vessels were identified as circular structures larger than 8 µm

in diameter surrounded by cells enclosing an empty space or only showing red blood cells within the structure, Figure 13. Occasionally, vessels were sectioned longitudinally; these were counted as one unless branches were visible. In this case, each branch was counted as one vessel.

4.4.4 Void Area

Masson's Trichrome staining was also used to measure the void, or blank, area of the scaffold. This gives a measurement of the overall density of the scaffold that can be correlated with MRI measurements of ADC and T_2. The same method was used to divide the scaffold into 10 equally sized regions as shown in Figure 11.

The void area of each region was measured and reported as a percentage of the total area. A macro was written for ImageJ to ensure consistent, repeatable results in a time effective manner. A schematic of the approach used in shown in Figure 14. Again, the images were split into hue, saturation and brightness stacks. The brightness stack was selected and the background image noise subtracted. The image was then converted to a binary image using threshold values that isolated the light regions from the remainder of the image. The percent of pixels that fell into the light category was measured. For complete details please see appendix for the code used.

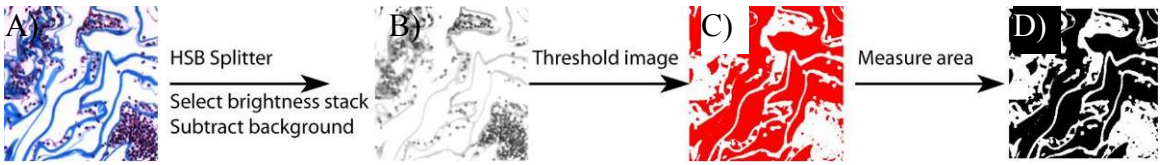

Figure 14: Semi-automated image analysis of MT stained region to measure void area
A ROI of an Masson's Trichrome (MT) stained section (A), was split into hue, saturation and brightness stacks. The brightness stack (B) was thresholded (C) and number of pixels thresholded were counted (D).

4.5 Correlation of MRI and Histology Data

MR images were acquired and analyzed by Kandasamy.[76] As part of the MRI analysis, scaffolds were divided into center and rim regions, as shown in Figure 15. These regions varied by implant and day on which the imaging was performed. Generally, the rim region consituted the outer fifth of the scaffold. To correlate these measurements with histology parameters, edge and core regions were defined as the outer 20% and middle 20% of the scaffold, respectively.

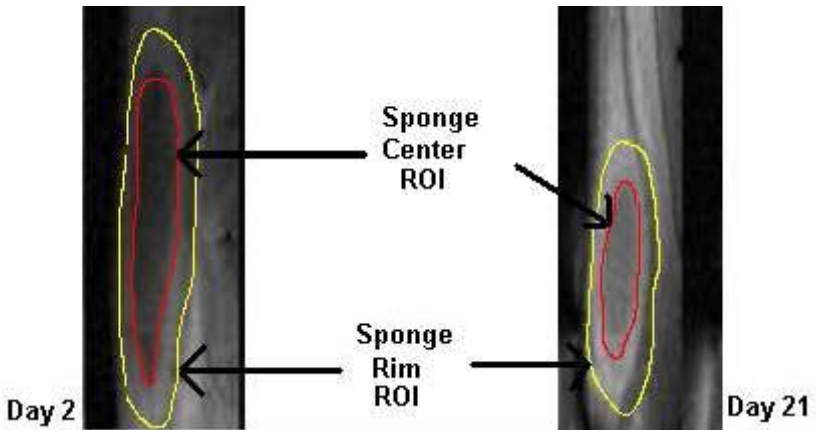

Figure 15: MR ROI selection
Contrast enhanced images of scaffold from Kandasamy,[76] showing how MRI ROIs were selected.

Correlations between the MRI data and histology data were performed by comparing MRI measurements taken immediately before the rat was euthanized with the histological measurements for each scaffold. Average scaffold values from MRI measurements of T_2, apparent diffusion coefficient (ADC) and volume for scaffolds were plotted against histology measurements of average cell density, void fractions and scaffold thickness. T_2, ADC, cell density and void fractions were averaged for the whole scaffold. Comparisons were made only in cases where histology and MRI data points were available for the same scaffold, reducing the total number of data points available.

5 Results

5.1 In Vitro Scaffold Degradation

Scaffolds were incubated in a proteolytic solution of bacterial collagenases to assess the effect the crosslinking treatment on the degradation of the scaffolds. The progression of scaffold degradation is shown in Figure 16. UnX scaffolds showed the first signs of degradation at 72 hours; by 96 hours they were noticeably fragmented (Figure 16D). The UnX scaffolds had reduced to fragments by 264 hours. In contrast,

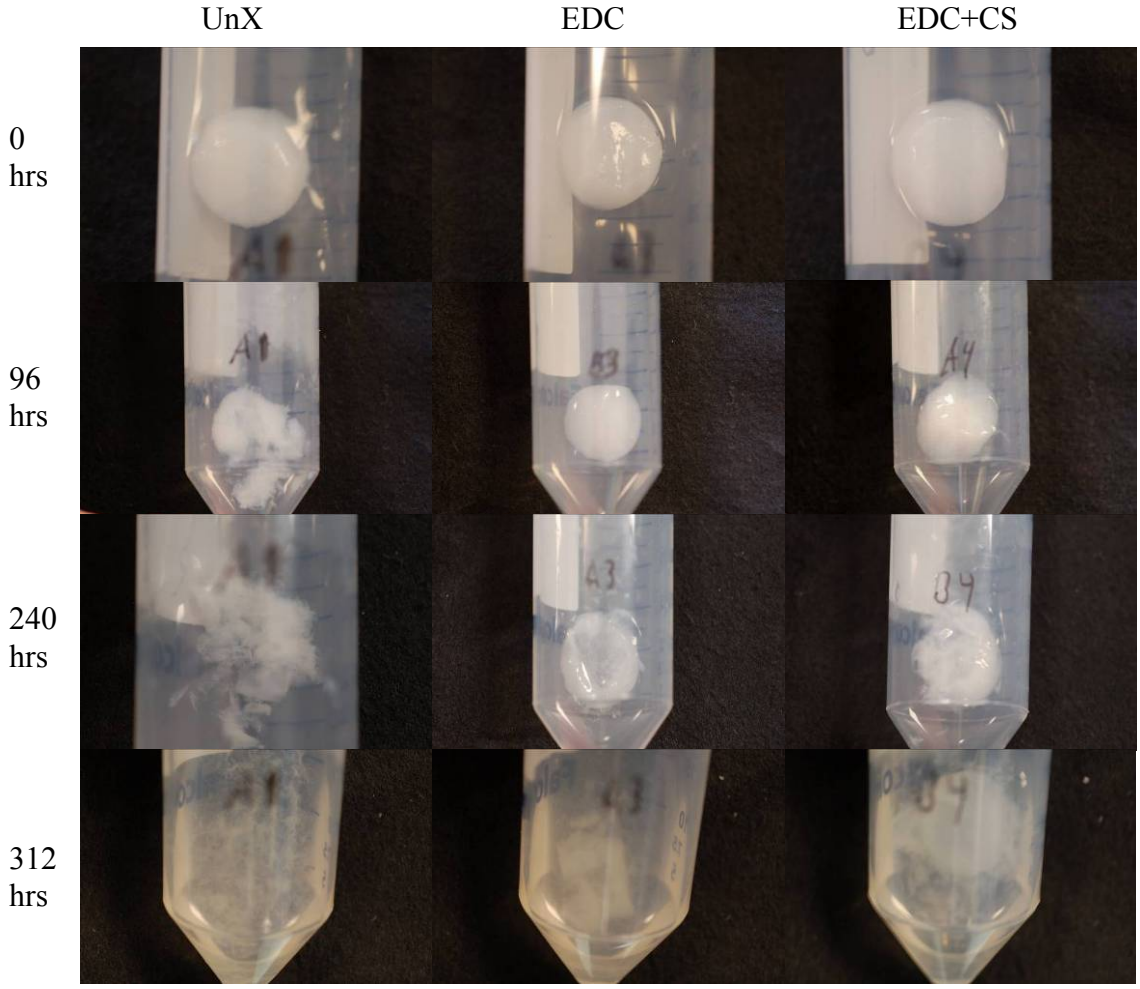

Figure 16: Scaffold degradation photographs showing scaffold degradation
A), D), G) and J) show UnX scaffolds at 0, 96, 240, and 312 hours respectively. B), E), H) and K) show EDC scaffolds at 0, 96, 240 and 312 hours respectively. C), F), I) and L) show EDC+CS scaffolds at 0, 96, 240 and 312 hours respectively. For size reference, all scaffolds were photographed in 50ml conical tubes (approximately 30mm in diameter).

the crosslinked scaffolds maintained their integrity until 240 hours (Figure 16H and I), and thereafter showed only slow and faint signs of structural collapse. By 312, hours the crosslinked sponges had completely fragmented, Figure 16K. Based on observations, it appeared that the EDC crosslinked scaffolds were slightly more resistant to degradation than the EDC+CS scaffolds and released fewer fragments into the solution at any given time point.

Supernatant samples were taken every 24 hours, while the scaffolds were degrading, and analyzed for hydroxyproline content. The results shown in Figure 17 indicate that the UnX scaffolds degraded quicker than the crosslinked ones. At all time points the UnX scaffolds had released more collagen into the solution. The

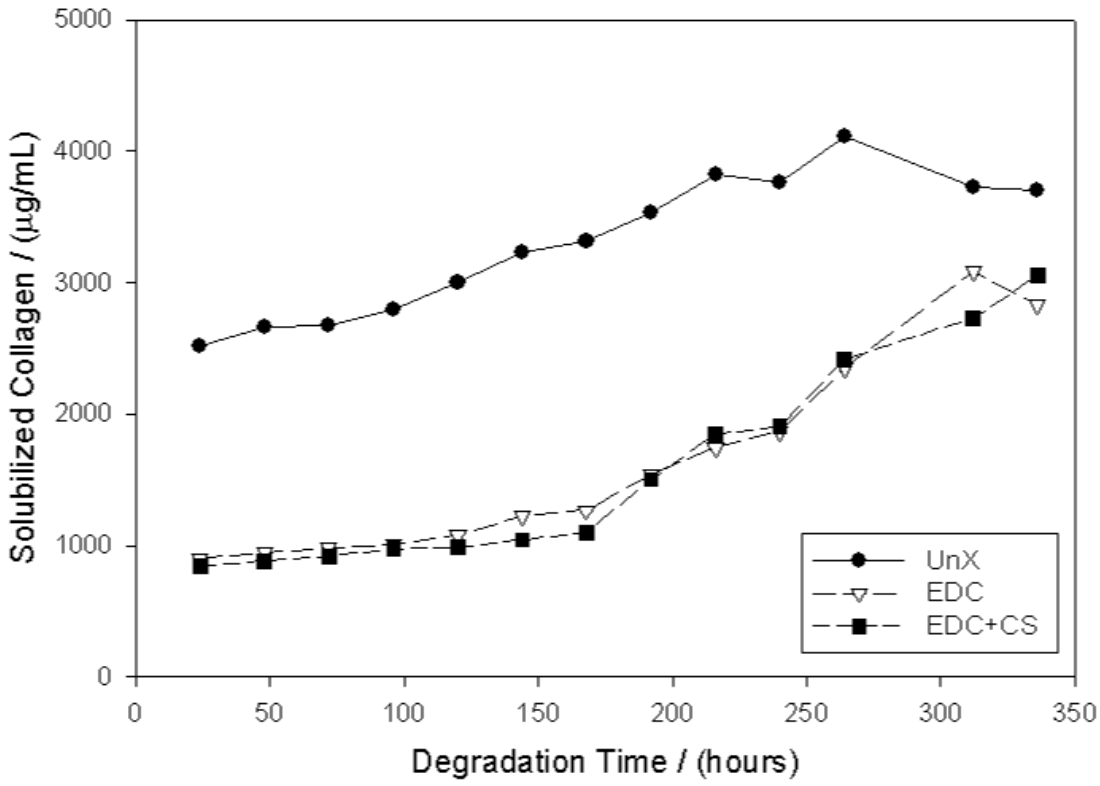

Figure 17: Plot of solubilized collagen released during degradation assay
Collagen scaffolds were exposed to bacterial collagenase and measures of hydroxyproline were correlated to solubilized collagen, results from one experiment, n = 2.

hydroxyproline measurements do not show any difference between the EDC- and EDC+CS-crosslinked scaffolds. The slight increased resistance to degradation of the EDC scaffolds based on observations of the structure and fragments, was not confirmed by the spectrophotometric measurement. Care should be taken interpreting these results due to the small sample size.

5.2 Histological Analysis

Scaffolds were implanted into dorsal subcutaneous pockets of rats to evaluate tissue responses. Rats were imaged using MRI and the scaffolds were harvested to assess cellular responses. Scaffolds harvested at Day 21 were infected and not processed for further analysis. Explants were stained with H&E and Masson's Trichrome and mosaic images of the thickness were created. The mosaic images, Figure 18,Figure 19 andFigure 20, show H&E sections of UnX, EDC and EDC+CS scaffolds, respectively. Masson's Trichrome mosaic images, Figure 21,Figure 22 andFigure 23 show UnX, EDC and EDC+CS scaffolds, respectively. All scaffolds showed an increase in cell number from the scaffold margin that gradually filled the entire thickness of the scaffold for all scaffolds by Day 14. UnX scaffolds had a greater number of inflammatory cells than crosslinked scaffolds. After 14 days, the majority of cells within the crosslinked scaffolds were non-inflammatory. After 14 days the UnX scaffolds had degraded completely (Figure 18) while the crosslinked scaffolds persisted to the last time point, 42 days (Figure 19F, and Figure 20F). Scaffold thicknesses decreased with time after day 14, for both crosslinking conditions, except for Day 42, where the scaffolds were thicker than those harvested at Day 35 (Figure 24).

Generally, UnX scaffolds had thicker capsules than crosslinked scaffolds at all time points. At Day 2 there was very little evidence of a capsule (Figure 21A, Figure 22A and Figure 23A). Capsule thickness increased up to Day 14, and then decreased as scaffold became integrated with the tissue. At Day 28, there was only a thin capsule surrounding the EDC scaffolds (Figure 22D). After this time point, the scaffolds had completely integrated with the surrounding tissue. EDC+CS scaffolds showed no capsule at Day 28 (Figure 23D), indicating quicker integration with the surrounding tissue.

The porous structure of the scaffolds was gradually filled with cells, connective tissue and blood vessels. UnX scaffolds appeared to degrade faster than new tissue grew in. In contrast, crosslinked scaffolds maintained their structure while the pores were filled by actively remodeling fibroblasts. The pores of EDC and EDC+CS scaffolds were completely filled by new tissue deposition by 28 and 35 days respectively, as seen by the increased staining of blue structures in Figure 23 E) and Figure 23D), indicative of new connective tissue synthesis.

The following sections provide quantitative analyses of changes in tissue responses that were measured as a function of scaffold crosslinking and implantation time.

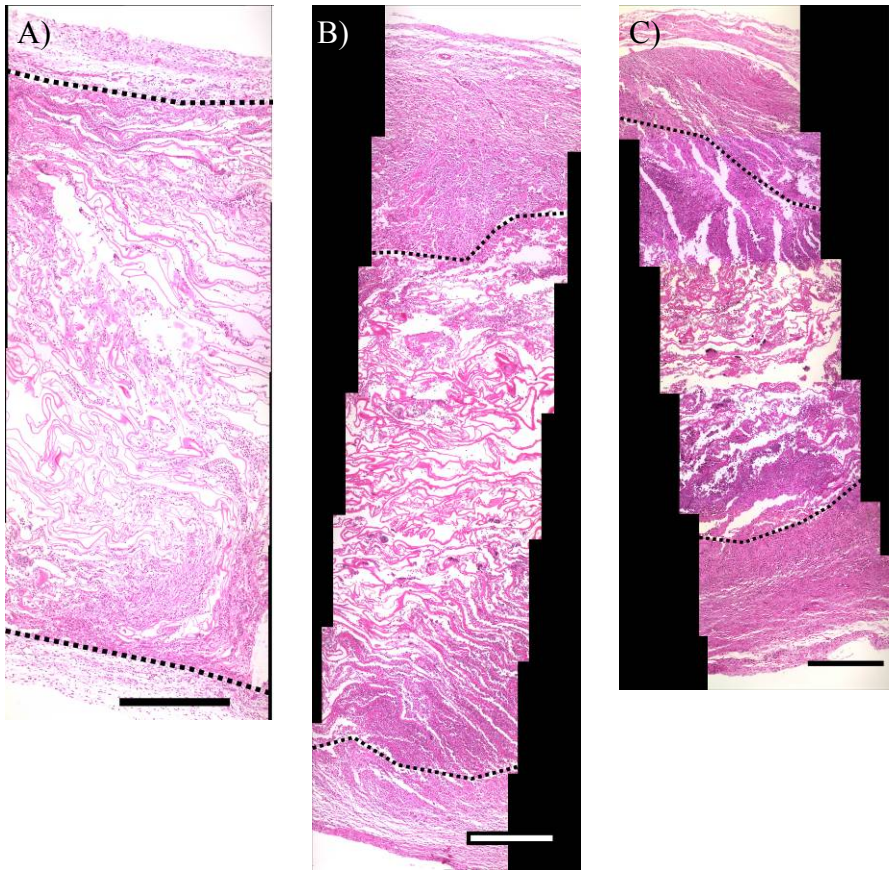

Figure 18: Mosaic photomicrographs of H&E sections of UnX scaffolds
Images show scaffolds at A) 2 days, B) 7 days and C) 14 days oriented with dorsal side up. Dotted line denotes margin between scaffold and surrounding tissue. Scale bar = 500 μm.

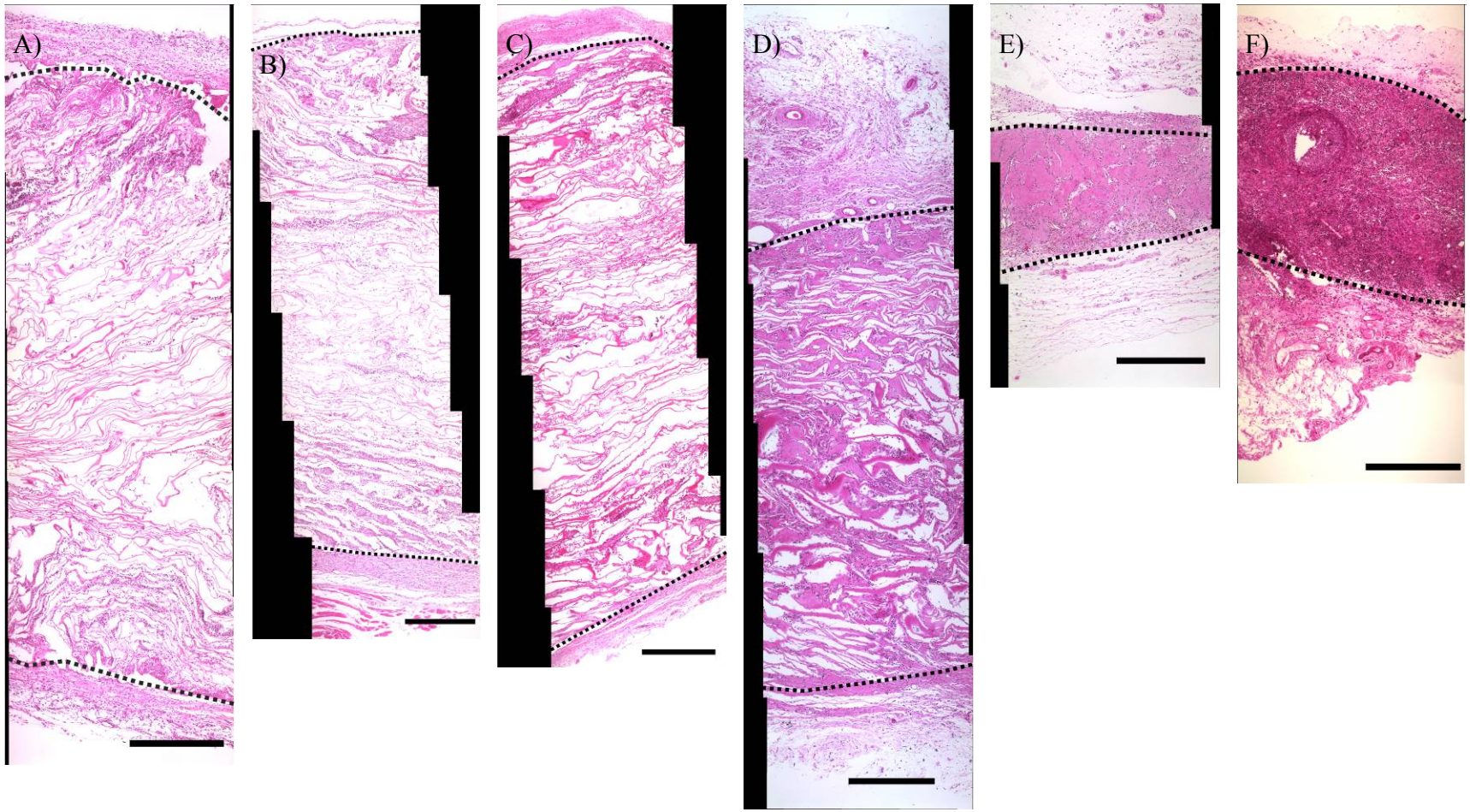

Figure 19: Mosaic photomicrographs of H&E sections of EDC scaffolds
Images show scaffolds at A) 2 days, B) 7 days, C) 14 days, D) 28 days, E) 35 days and F) 42 days oriented with dorsal side up. Dotted line denotes margin between scaffold and surrounding tissue. Scale bar = 500 μm.

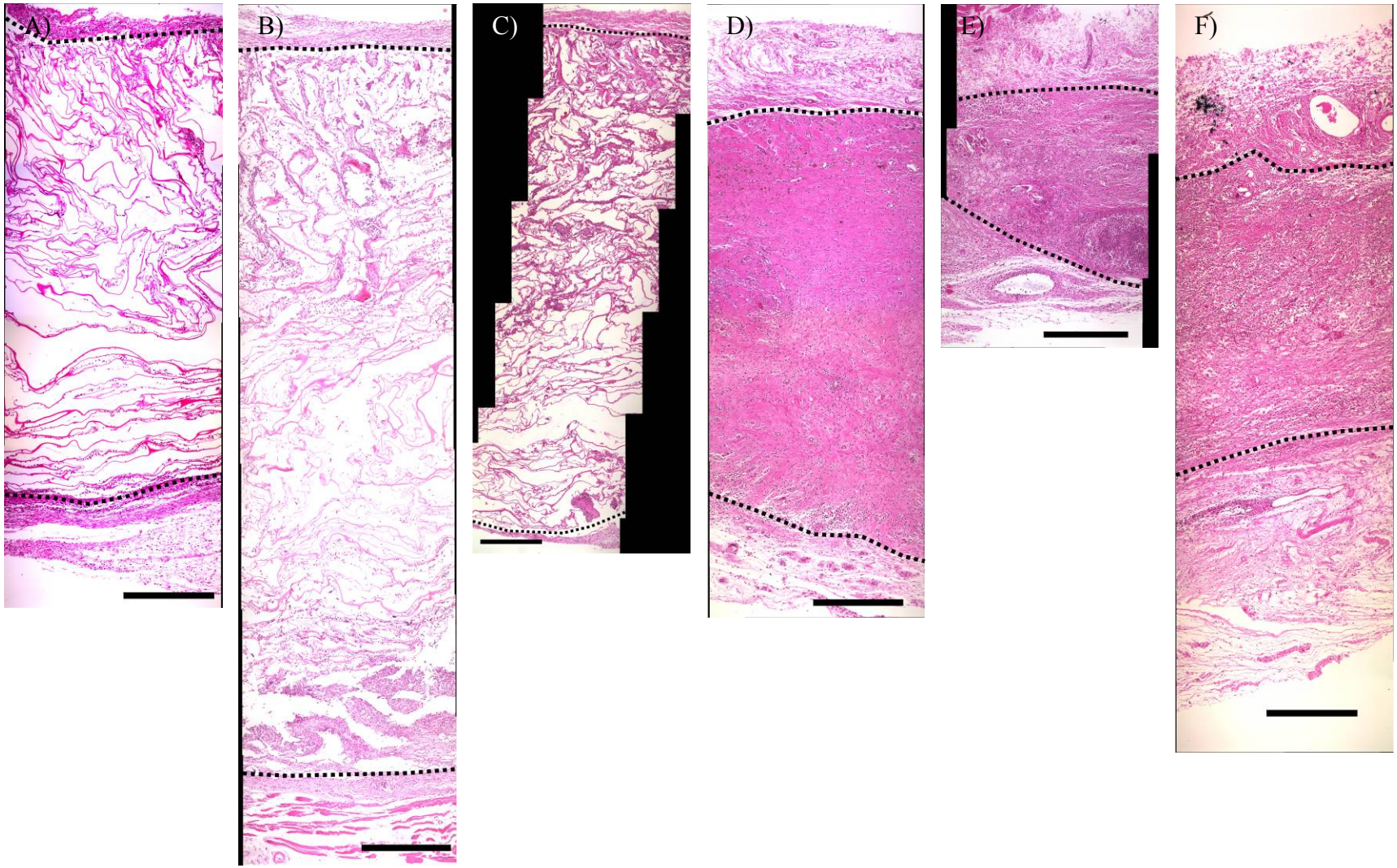

Figure 20: Mosaic photomicrographs of H&E sections of EDC+CS scaffolds
Images show scaffolds at A) 2 days, B) 7 days, C) 14 days, D) 28 days, E) 35 days and F) 42 days oriented with dorsal side up. Dotted line denotes margin between scaffold and surrounding tissue. Scale bar = 500 µm.

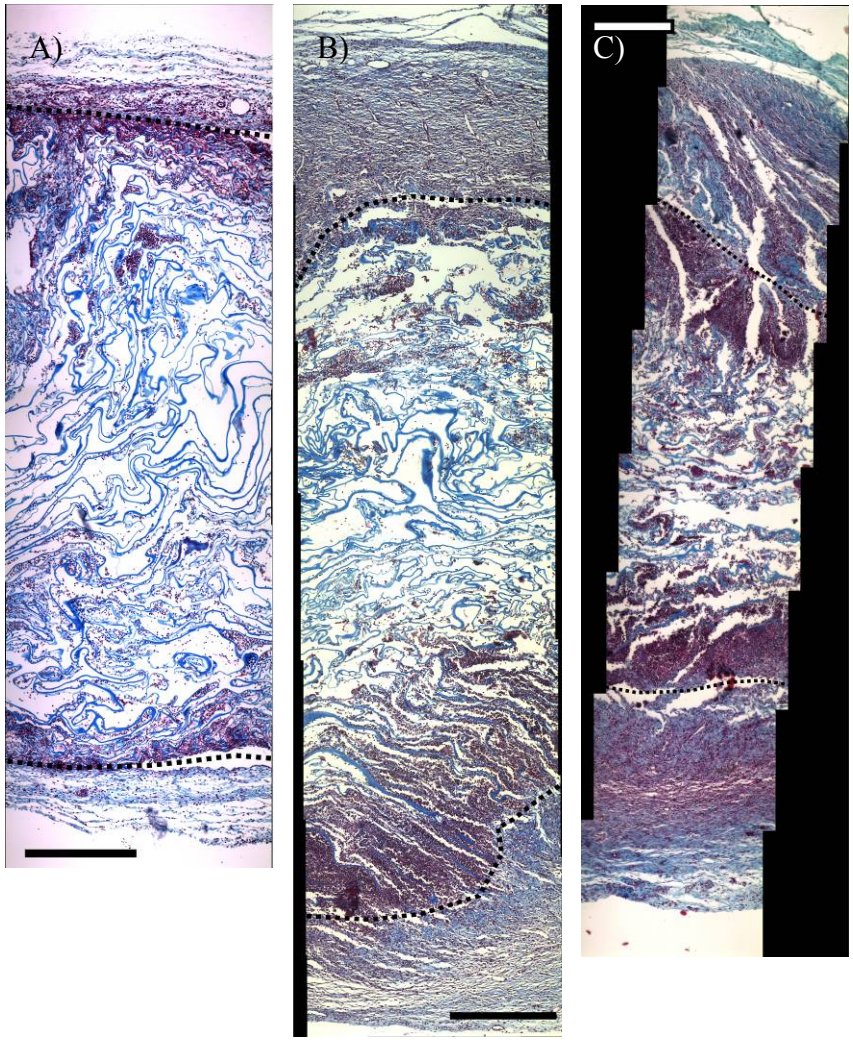

Figure 21: Mosaic photomicrographs of Masson's Trichrome sections of UnX scaffolds
Images show scaffolds at A) 2 days, B) 7 days and C) 14 days oriented with dorsal side up. Dotted line denotes margin between scaffold and surrounding tissue. Scale bar = 500 μm.

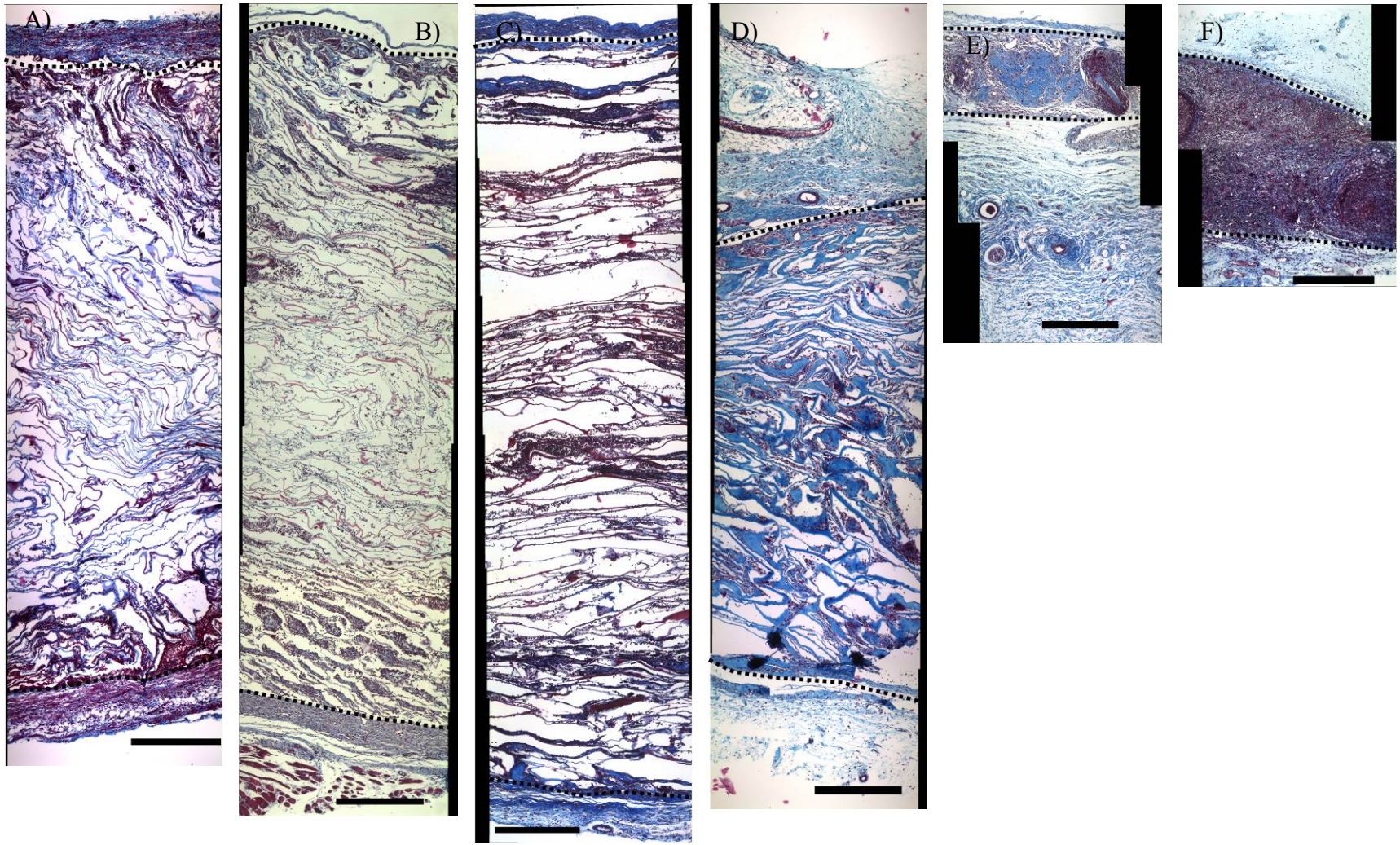

Figure 22: Mosaic photomicrographs of Masson's Trichrome sections of EDC scaffolds
Images show scaffolds at A) 2 days, B) 7 days, C) 14 days, D) 28 days, E) 35 days and F) 42 days oriented with dorsal side up. Dotted line denotes margin between scaffold and surrounding tissue. Scale bar = 500 µm.

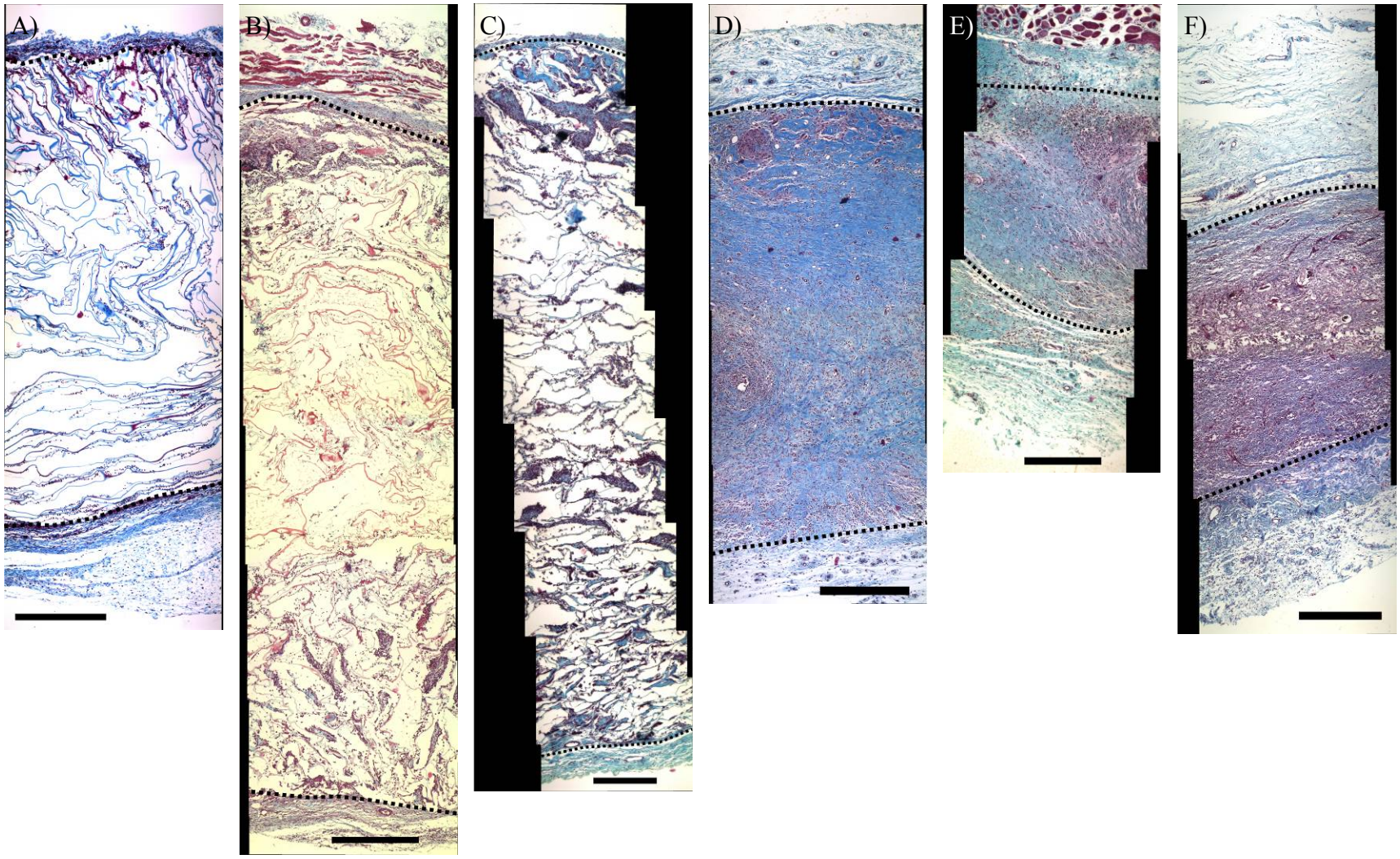

Figure 23: Mosaic photomicrographs of Masson's Trichrome sections of EDC+CS scaffolds
Images show scaffolds at A) 2 days, B) 7 days, C) 14 days, D) 28 days, E) 35 days and F) 42 days oriented with dorsal side up. Dotted line denotes margin between scaffold and surrounding tissue. Scale bar = 500 µm.

5.2.1 Thickness

Scaffold thicknesses were measured using the mosaic images to quantify the change in size of the scaffolds to correlate with the MRI measurements of scaffold volume. The results are shown in Figure 24. These measures show an increase in crosslinked scaffold volume at Days 7 and 14, that is more marked for EDC+CS scaffolds than EDC. After Day 14, the scaffold thicknesses decrease with implantation time, except for Day 42 where there is a slight increase. UnX scaffolds show greater capsule thicknesses than crosslinked scaffolds at Day 7 and 14, but not Day 2. By Day 28, there is only a very thin capsule present around the EDC scaffolds, approximately 50 μm, while the EDC+CS scaffolds show no evidence of a capsule after Day 14.

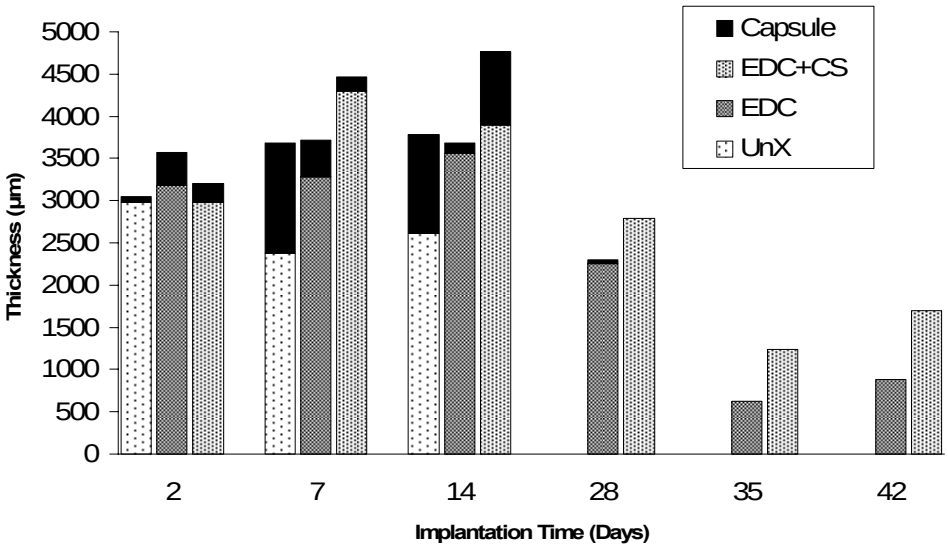

Figure 24: Scaffold thickness as a function of implantation time
n = 2 for all bars.

5.2.2 Cellular Density

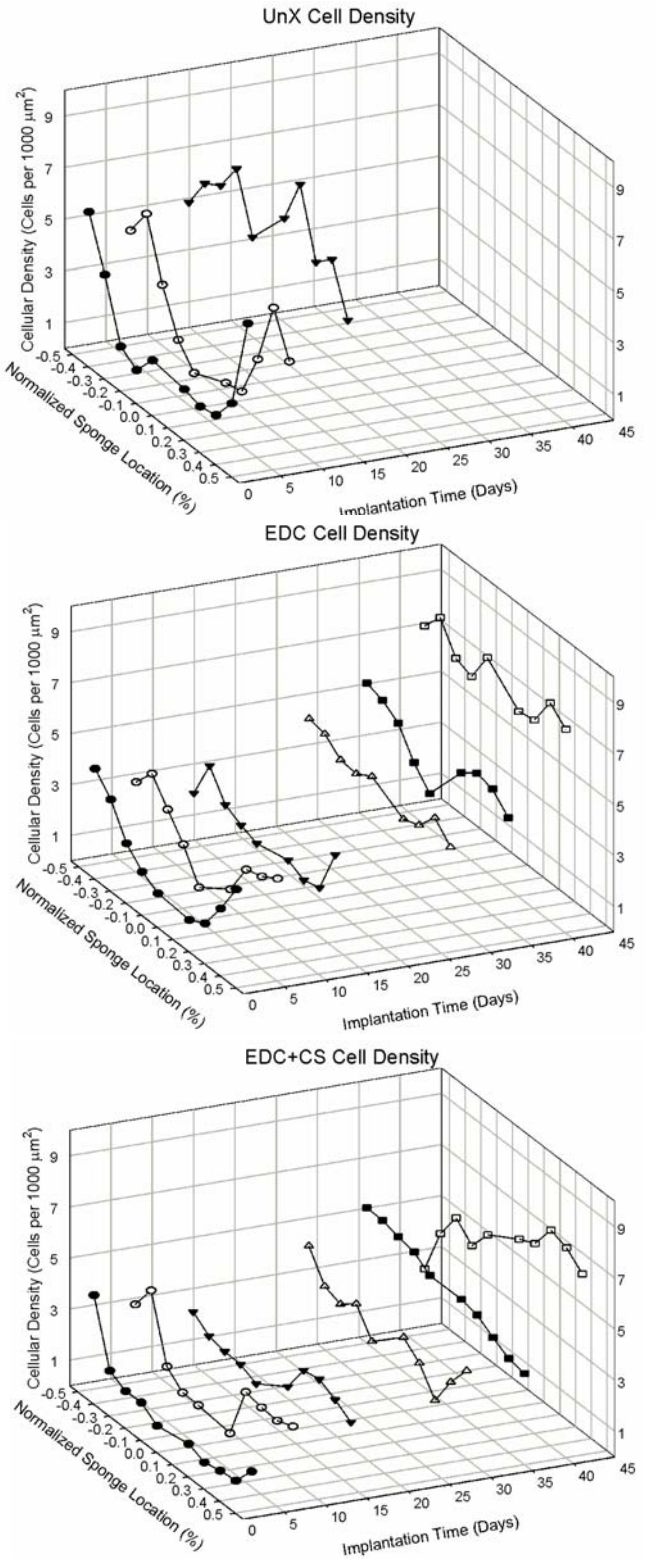

Figure 25: Plots of cellular densities for UnX, EDC and EDC+CS scaffolds as a function of scaffold location and implantation time
For all plots n = 2

Cellular infiltration into the scaffolds was measured by counting the number of cells within regions taken across the thickness of the scaffold to determine the cellular density at various depths within the scaffold. Region size was normalized to the total thickness of the scaffold to ensure an equal number of measurements were taken from each scaffold, despite greatly varying sizes. The results obtained for cellular density for the three types of scaffolds are shown in Figure 25.

These plots show a general increasing trend in cell numbers with increasing time for all scaffolds. Cellular density is initially high at the scaffold margins and increases in the core regions of the scaffold with longer

implantation times. Cell density at the margins of UnX scaffolds is higher than crosslinked sponges at 2, 7 and 14 days. This is consistent with qualitative observations from Figure 18. UnX scaffolds also show a faster increase in cellular density in the core regions compared to crosslinked scaffolds at Day 14.

EDC scaffolds had cellular densities that were lower than UnX, but slightly higher than EDC+CS scaffolds, particularly at Day 2. This trend continued until Day 35, where the EDC+CS showed a relatively homogenous distribution of cells, whereas the EDC scaffolds still had a markedly reduced density at the core regions on Day 35. By Day 42, the cellular densities of the two crosslinked scaffolds were similar, with the EDC+CS scaffolds having fewer cells on the ventral side of the scaffold. Besides this one case, the cellular infiltration appears to occur at a similar rate from both directions into the scaffold, resulting in a mostly symmetrical distribution of cells at any given time point.

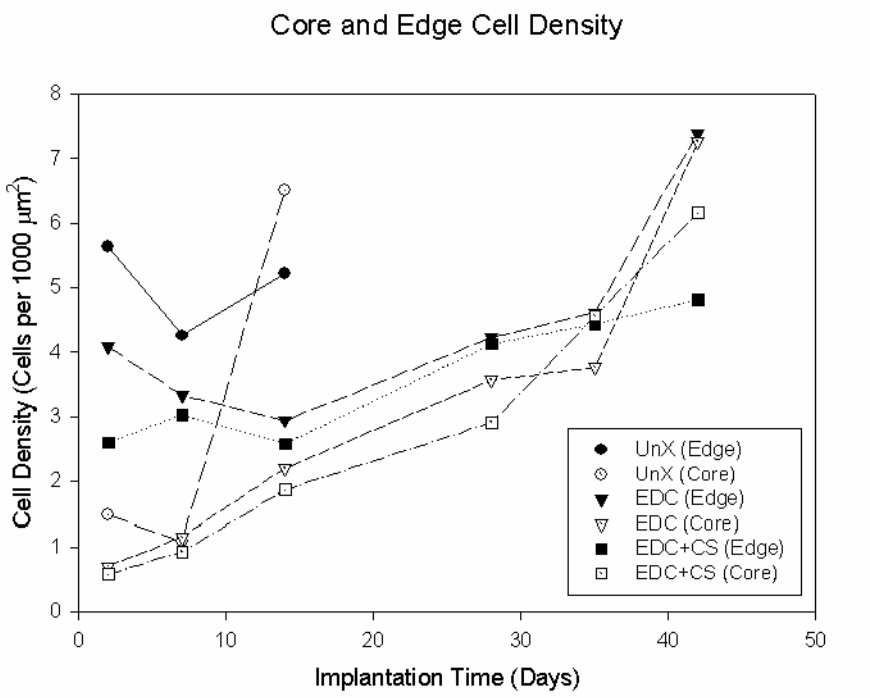

Figure 26: Core and edge cell density
Each point is an average of outer and middle 20% of scaffold (4 measurements per data point, n = 2)

The cellular densities of the edge and core regions (20% of total scaffold thickness for each region were compared for various scaffolds), and the results are shown in Figure 26. This figure shows more clearly the increased cell density at the scaffold edges, compared to the core regions. The steady increasing trend of cells at the core of the scaffold is also observed, with core regions exceeding the cell density of the edge by Days 14 and 42 for UnX and EDC+CS scaffolds respectively. EDC scaffolds show equal cell densities at Day 42. Cellular densities at the edge of the crosslinked scaffolds decreases between day 7 and 14. Again, UnX scaffolds show higher cell numbers than both crosslinked scaffolds and EDC scaffolds had marginally higher cell densities than EDC+CS scaffolds. By Day 35, there is very little difference in cell density between the edge and core regions of the scaffolds.

5.2.3 Blood Vessel Density

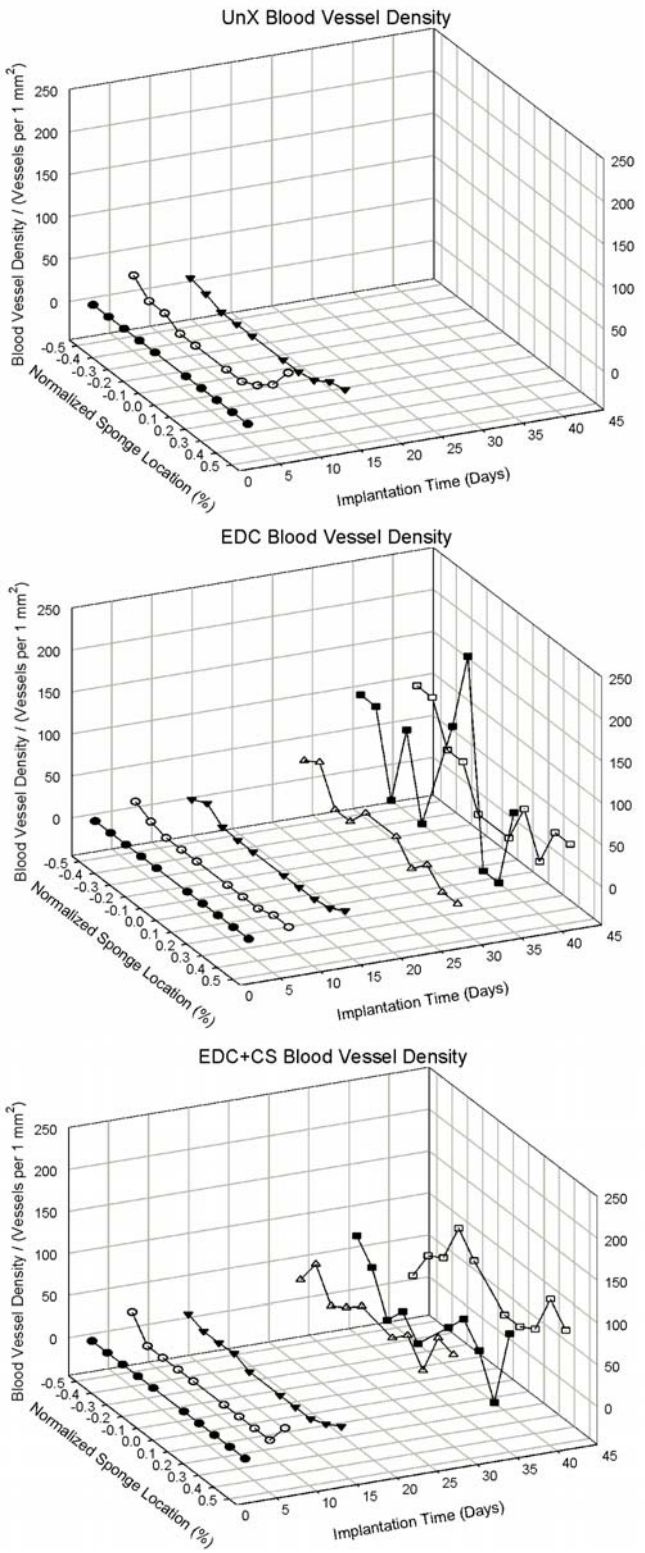

Figure 27: Blood vessel densities for UnX, EDC and EDC+CS scaffolds as a function of scaffold location and implantation time
For all plots n = 2

Angiogenesis within the scaffolds was measured by counting the number of blood vessels within regions, across the thicknesses of the scaffolds using the Masson's Trichrome mosaics. The results obtained are shown in Figure 27.

No blood vessels were seen at Day 2 in any of the scaffolds. At Day 7, UnX showed the greatest vascularity, which reduced by Day 14 at the margins. No blood vessels were seen in the center of the UnX scaffolds at any time point.

Crosslinked scaffolds showed an increase in blood vessels with implantation time. At Day 28, there were more blood vessels in the EDC+CS scaffolds than in the EDC. By Day 28, there were still regions of the EDC scaffold that did not contain any blood vessels. However, at Day

42, there were a remarkable number of blood vessels at the center of the EDC scaffold. All regions of the EDC+CS scaffolds showed evidence of blood vessels by Day 28. By Day 42, there was a somewhat homogenous distribution of blood vessels within the EDC+CS scaffolds.

Vessel densities for edge and core regions were plotted in Figure 28. There was a general increasing trend for blood vessels in both edge and core regions for all scaffold types with increasing implantation time. UnX scaffolds only showed blood vessels at the edge of the scaffold, whereas crosslinked vessels showed steadily increasing vessel densities throughout the scaffold. The EDC+CS scaffolds showed higher vessel densities at both the edge and center compared to EDC scaffolds for most time points. However, no blood vessels were seen at the center of the EDC+CS scaffolds at Day 42. Both EDC and EDC+CS scaffolds showed a decrease in vessel density between Days 35 and 42.

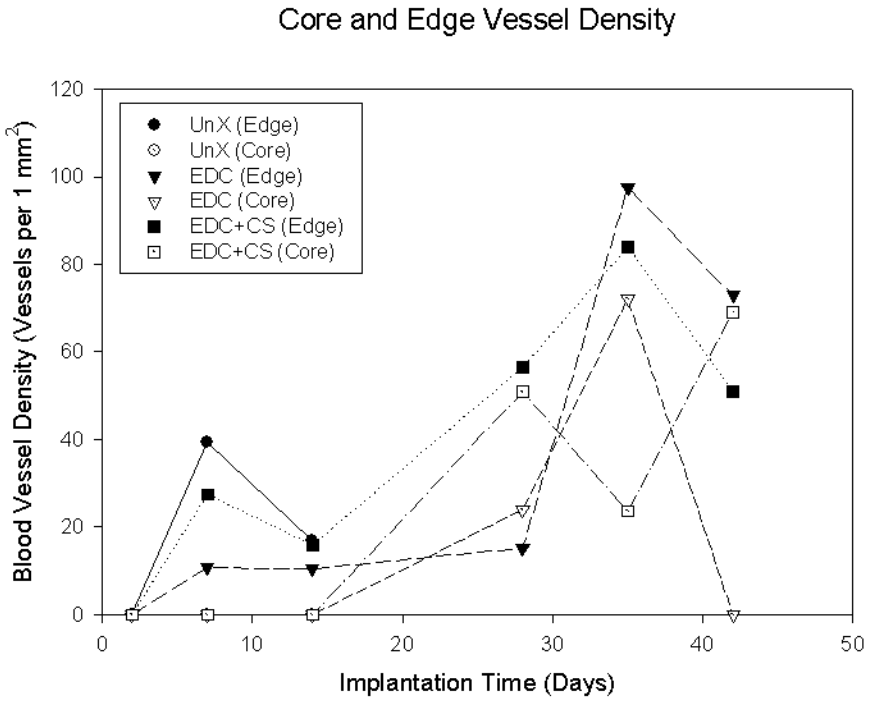

Figure 28: Core and edge vessel density
Each point is an average of outer and middle 20% of scaffold (4 measurements per data point, n =2)

5.2.4 Void Area

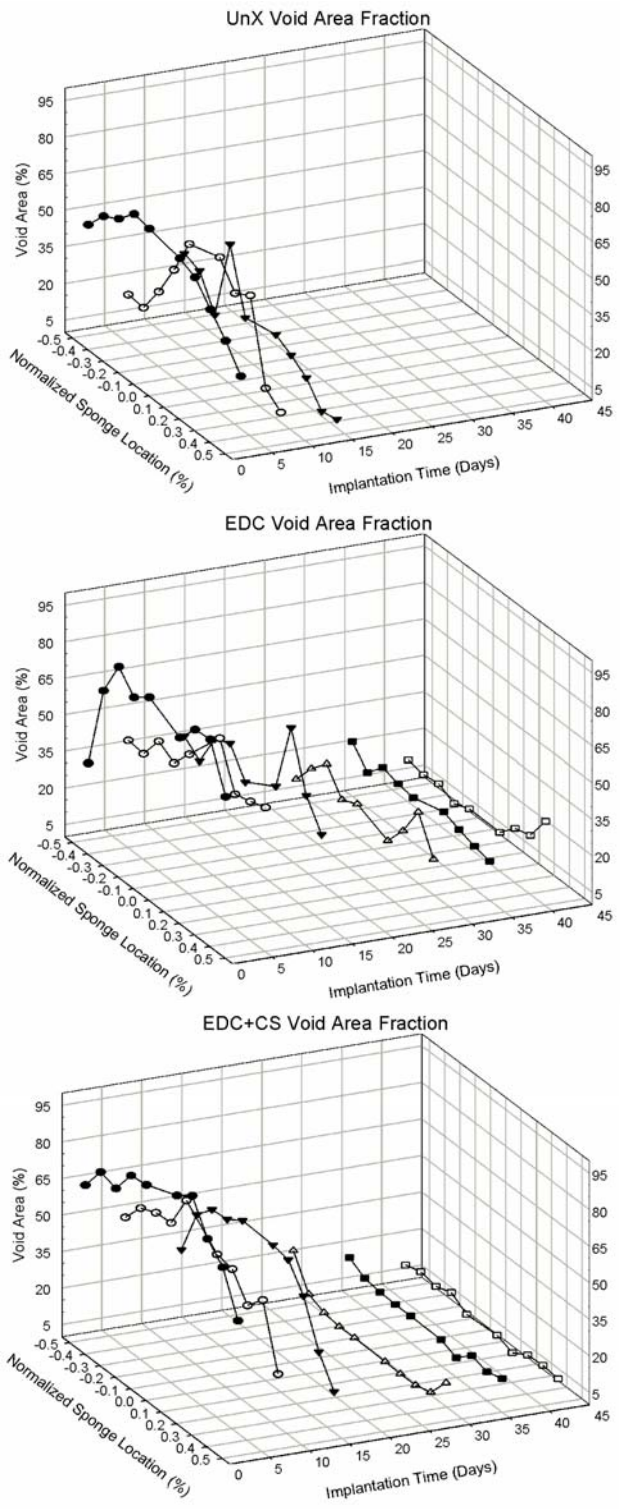

Figure 29: Void area fractions for UnX, EDC and EDC+CS scaffolds as a function of scaffold location and implantation time
For all plots n = 2

The void area fraction of each scaffold was measured to quantify the overall tissue ingrowth into the scaffolds. Figure 29 shows the void area percentages for all scaffold types as a function of implantation time and scaffold location.

All scaffolds show a decrease in the void fraction with increasing implantation time. At early time points, void areas were lower at the edges of the scaffolds, compared to the central regions, with a fairly symmetrical profile. At Days 28 and 35, this profile had reversed itself in the EDC+CS scaffolds, with greater void areas at the edges.

UnX scaffolds showed a reduced tendency to become filled and maintained a steeper gradient between the edges and central regions

compared to the crosslinked scaffolds, where the profile had flattened considerably even by Day 7.

EDC+CS scaffolds reached a minimum void area by Day 28 in the central regions that persisted until Day 42. EDC scaffolds only reached the same level by Day 42, whereas UnX scaffolds never reached this minimum.

Figure 30 shows the void area fractions of the edge and core regions of the scaffolds as a function of scaffold type and implantation time. This plot shows the same decreasing trend for all scaffold types at the edge and core regions. UnX scaffolds have lower void fractions in the core regions compared to the core regions of crosslinked scaffolds, but they are never less than 20%. The edges are likewise more filled. Void fractions at the edge regions of EDC scaffolds increase slightly between Days 2 and 7, and remain unchanged until Day 14, before decreasing to levels similar to EDC+CS

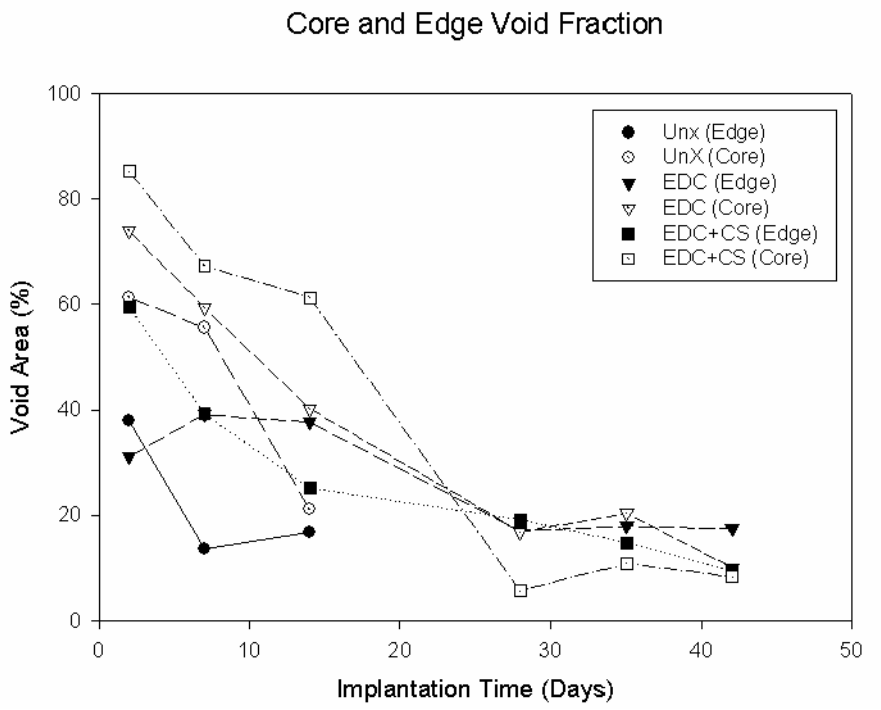

Figure 30: Core and edge void area fraction
Each point is an average of outer and middle 20% of scaffold (4 measurements per data point, n = 2)

scaffolds. EDC+CS scaffolds have a higher initial void fraction at Day 2 that persists through Day 14. At later times, there is a marked decrease, particularly in the core region between Days 14 and 28. After Day 28, there is little change in the void area, and there are only small differences between edge and core regions of the scaffolds.

5.3 MRI Correlations

MRI measurements taken immediately before scaffolds were harvested were plotted against histology measurements of the same scaffolds in various combinations of parameters to explore the correlations between the two sets of data. Scaffolds were only included if both MRI and histology data was available (21 scaffolds total). Figure 31 shows these results graphically and the statistical results are summarized in Table 2.

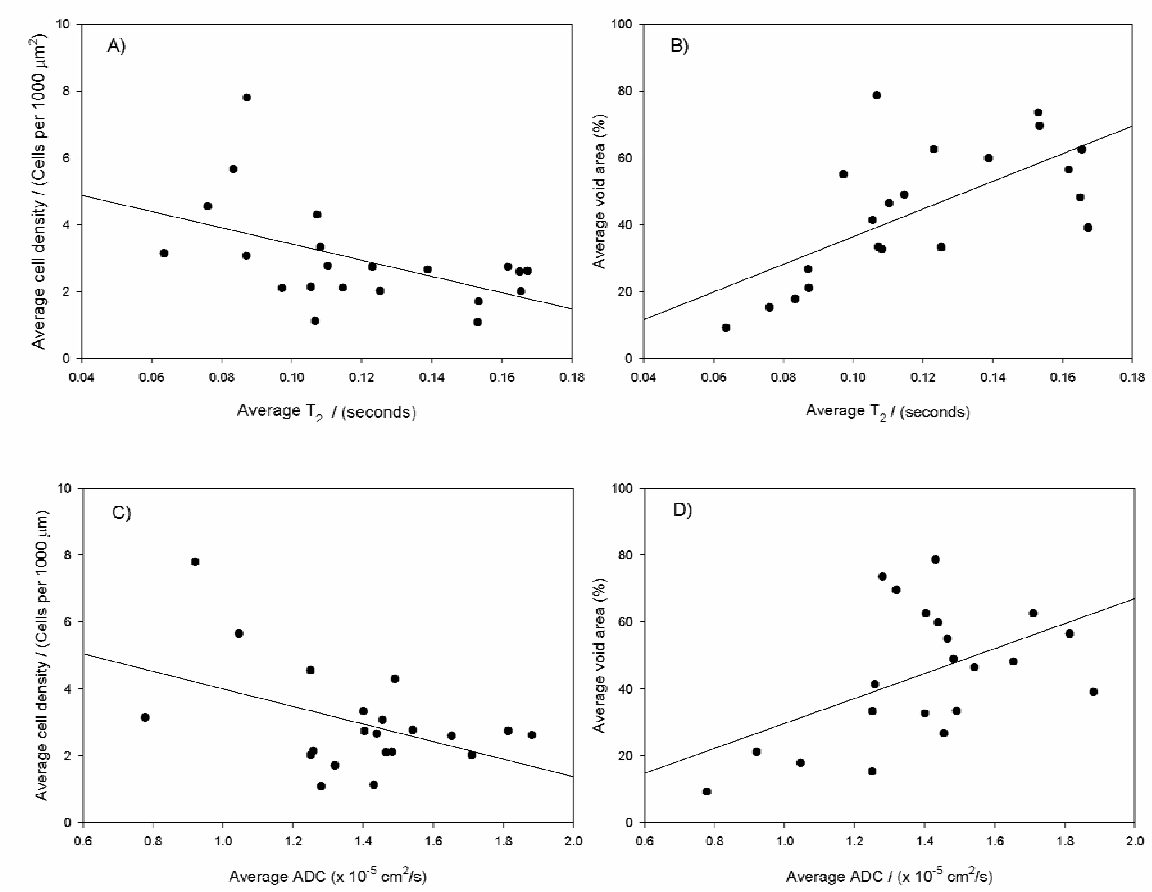

Figure 31: Correlations between histology and MRI measurements
Each point represents measurements taken from one scaffold, where the x-axis represents the MRI measurement and the y-axis represents the histology measurement. A total of 21 scaffolds used for each scatter plot.

The correlation between average cell density and average T_2 values, (Figure 31A) shows longer T_2 relaxation times are generally associated with lower cellular densities, and the correlation appears better at longer T_2 values. Void area and ADC are positively

correlated, as are void area and average T_2 value. The strongest correlation was seen between void area and T_2 (Figure 31B).

The Pearson product moment correlation for these combinations were computed. These results show that statistically significant ($p < 0.05$), linear relationships exist between T_2 and cell density, ADC and cell density, T_2 and void area, as well as ADC and void area (Table 2). The best correlation is seen between void area and T_2. ADC and cell density have the weakest correlation.

Table 2: Correlation statistics summary

		MRI Parameter	
	n = 21	T_2	ADC
Histology Parameter	Cell Density	r = -0.503 p = 0.02	r = -0.455 p = 0.04
	Void Area	r = 0.666 p < 0.0001	r = 0.502 p = 0.02

To show the robustness of the linear regressions, plots of the residuals are shown in Figure 32 and were used to evaluate the quality of the fit. Based on inspection, each shows a slight linear trend in the residuals. This suggests that the model does not fit the data appropriately. The residuals should be randomly distributed for a good fit. The observations are plotted in order of increasing implantation time.

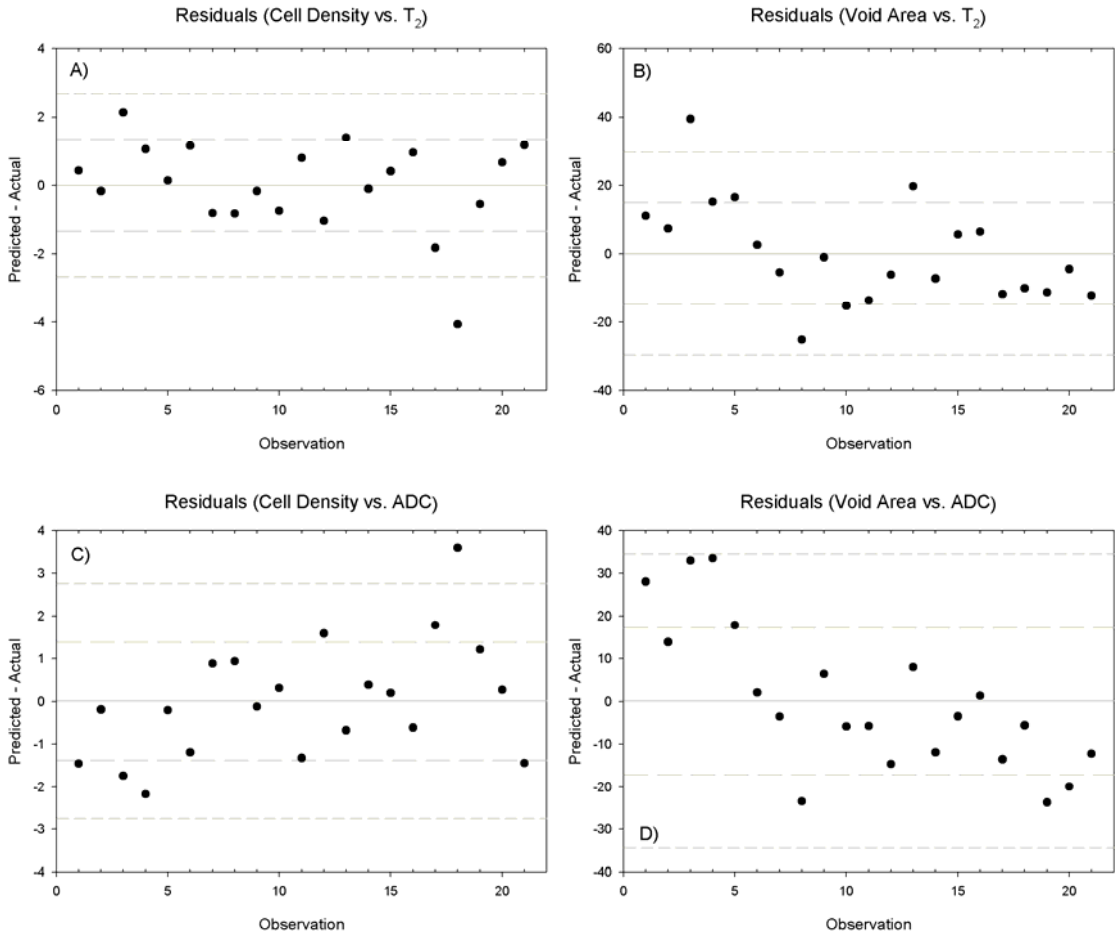

Figure 32: Residual values from correlations
Difference between predicted and actual values for (A) Cell density and (B) Void area using T_2, (C) Cell density and (D) Void area using ADC. Long dash shows one standard deviation, short dash shows two standard deviations.

6 Discussion

The goal of this study was to characterize the cellular response and remodeling processes that occur within collagen scaffolds after implantation and correlate these results with MRI measurements; working towards developing MRI methodologies that can be applied to noninvasively monitoring tissue responses to implants. To study these relationships, the effects of crosslinking treatments and conjugation of GAG (CS) to collagen scaffolds were explored, as well as the *in vitro* degradation rates.

6.1 In Vitro Scaffold Degradation

The resistance of scaffolds to degradation, as measured by the amount of hydroxyproline solubilized when scaffolds were treated with bacterial collagenases, showed that the uncrosslinked scaffolds degraded faster than both crosslinked conditions. These observations are consistent with previous data on the effects of EDC crosslinking of collagen[22,32,82,83] and other materials.[25,84,85] The addition of chemical bonds between collagen molecules increases the number of chain cleavages that must be performed by the enzyme to compromise the structural stability of the scaffold and liberate peptides. Despite the fact that EDC is a "zero-length" crosslinker and will only crosslink molecules that are within a few angstroms of each other, a sufficient numbers of bonds are formed to noticeably strengthen the material. The EDC crosslinking reagent, 1-ethyl-(3,3-dimethylaminopropyl)-carbodiimide, undergoes a reaction that effectively creates a peptide bond between two proteins. This reaction would likely occur spontaneously under aqueous conditions, but at a much slower rate.

Unexpectedly, there was no detectable difference in the degradation between the EDC and EDC+CS scaffolds. The fact that the crosslinker itself is consumed in

conjugating the chondroitin sulfate to the collagen matrix, should reduce the number of available reaction sites to crosslink collagen molecules. Previous research has indicated that this is indeed the case and lower resistances to degradation are obtained when CS was incorporated, but this was not a statistically significant difference.[86] In a separate study, a secondary crosslinking step attached the CS, after first crosslinking the collagen matrix itself.[26] This resulted in collagen-CS matrices that were more resistant to degradation than matrices crosslinked once with EDC alone.

6.2 Histological analysis

6.2.1 Thickness

Scaffold thicknesses generally showed a decreasing trend with increasing implantation time regardless of crosslinking technique. This result is consistent the expected outcomes. The wound environment created by the surgery and the associated inflammatory response to both the surgery and the foreign material, as well as the continuous remodeling processes that occur within the rat once the inflammation has resolved, all involve the release of proteolytic enzymes that serve to degrade the collagen scaffolds.[10] The initial inflammatory response, minutes to hours after the scaffold has been implanted, involves the release of non-specific lysosomal proteases and oxygen-derived free radicals from damaged cells and neutrophils that degrade most protein materials, including potentially infectious microbes. Later in the inflammatory response, macrophages secrete neutral proteases that further degrade the scaffold.[87] After the inflammatory response, normal tissue remodeling processes involving the regulation of very specific matrix metalloproteinases (MMP) by tissue inhibitors of metalloproteinase (TIMP), cause the decrease in scaffold size. Collagenase MMPs, such as MMP-1,-8,-

13,and -18 have all been show to act on collagen substrates to breakdown these proteins.[88] While these enzymes are very substrate specific, the structural homology of collagen types between species allows the native rats enzymes to still use the bovine collagen as a substrate. Overall, the degradation rates appeared to be slightly faster compared to Pieper *et al*., the where the scaffolds were still present after 10 weeks.[37]

The scaffold thicknesses, even at Day 2, were greatly reduced from the initial thickness of approximately 1 cm. This is primarily due to the compressive forces placed on the scaffold by the surrounding tissue, namely the skin. The compressive modulus of these materials is very low and has been reported to be on the order of 1kPa and 150Pa for EDC+CS and uncrosslinked scaffolds, respectively.[29] The presence of CS was also associated with a slight increase in thickness. This can be explained by the fact that hydrophilic charge groups on the surfaces of the GAG are responsible for increased water content in cartilage based on the electrostatic forces that cause water molecules to arrange in shells around the long GAG chains.[89] These same electrostatic forces would lead to a slight swelling of EDC+CS scaffolds compared to EDC and uncrosslinked scaffolds.

The thicknesses of the capsules surrounding UnX scaffolds were usually much thicker than those surrounding the crosslinked scaffolds. This is thought to be due to the increased release rate of protein fragments over the crosslinked scaffolds that the inflammatory cells respond to that increases the cellular activity to isolate the implant.[87] Furthermore, crosslinking has been shown to reduce the immunogenicity of collagen, [7] which may also be a contributing factor at time points after 2 days.

The MRI measurements of crosslinked scaffolds indicated an increase in volumes for all scaffold types at Day 7. This is consistent with the thickness measurements in this

study. At Day 14, the crosslinked scaffolds had returned to values close to their initial volume, and showed a decreasing trend at later time points. The same decrease was observed in the scaffold thicknesses of the crosslinked sponges, except for scaffolds harvested at Day 42. EDC+CS scaffolds were generally thicker than EDC at all time points except Day 2, however, EDC scaffold volumes were higher than EDC+CS. The thickness measurements are also influenced by the various processing steps (fixing, embedding, sectioning) that the scaffolds go through before they are placed under the microscope. Sectioning artifacts, such as separation of tissue layers or compression, may also have added variability to the data.

6.2.2 Cellular Density

Cellular density within the scaffolds was measured as a function of location with the scaffold by counting the number of nuclei present within ROIs. The uncrosslinked scaffolds showed greater cell density at the edges of the scaffold than the crosslinked scaffolds at the three time points they were harvested (2, 7, and 14 days). This result is thought to be part of the same increased inflammatory response that contributed to a thicker capsule. Pieper *et al.* also reported a decrease in cell density for crosslinked scaffolds between 2 and 4 weeks that was not observed in this study.[37] A qualitative change was observed in the predominant cell type present in the crosslinked scaffolds, from inflammatory cells to fibroblasts with increasing implantation time. The change in the cell population is expected to reduce the total cellularity, but this was not observed.

Cellular migration into the scaffolds and the establishment of a homogenous cell population occurred in the EDC+CS scaffolds sooner than in the EDC. These results are consistent with other reports of improved tissue ingrowth and cellular response of

collagen-GAG matrices over unmodified collagen.[33,34,90-92] The cells also had further to infiltrate as the EDC+CS were slightly thicker, at all time points. The exact mechanism by which CS improves cellular infiltration is still not clear. Explanations include the binding of CS to a wide range of proteins (proteases, growth factors, other ECM components, morphogens); either sequestering them or presenting them to the cells, resulting in changes of cell behavior.[35] The variations in GAG structure and the multitude of proteins with which they interact make their full characterization difficult. The binding of CS to basic fibroblast growth factor (bFGF) has been shown to play a role in the binding of bFGF to the surface receptors on the cell surface that actually lead to a change in cell function.[93] This could be occurring with any number of endogenous growth factors. As a natural part of the normal ECM, it is expected that cell function and biocompatibility would be improved by the presence of CS.

The metric for cellular density used in this study is based on total cellularity and does not take into consideration the type of cell present. The population sizes of neutrophils, macrophages, leukocytes, giant cells and fibroblasts, as well as the relative numbers of each type of cell, are considered important when evaluating the overall biocompatibility of a material.[39] However, for the purposes of this study, total cell populations are considered suitable because conventional MRI is not able to distinguish differences in cell population. There has been some investigation into using ^{1}H NMR spectroscopy to distinguish between types of cells based on differences in cell metabolites, but this work is beyond the scope of this thesis.[94]

MRI measurements of T_2 values of the scaffold showed regions of short and long T_2 at Days 2, 7, and 14 for all scaffolds. The long T_2 values, observed in the core regions

of the scaffolds, gradually decreased with implantation time until they were indistinguishable from the short T_2 regions. This is consistent with cellular infiltration and tissue ingrowth into the scaffolds and the establishment of a homogenous cell population. The average T_2 values for all scaffolds decreased until Day 21, at later time points they remain relatively constant. ADC measurements showed a similar decrease up to Day 21, and then remained constant at later time points, corroborating the T_2 observations.

6.2.3 Blood Vessel Density

EDC+CS scaffolds showed the greatest development of a vascular network, and had the greatest vessel density at the end of the study. These observations are consistent with expected results and previous reports of improved angiogenesis in the literature when chondroitin sulfate or other GAGs are present.[37,95,96] The increased number of blood vessels at the margins of UnX scaffolds was associated with elevated cell densities. The angiogenic potential of uncrosslinked collagen scaffolds, while slightly greater at the edges than crosslinked sponges, is not particularly remarkable given its instability and compared to what can be achieved by various modifications, such as the incorporation of growth factors[97]. The higher cell densities result in the release various chemotractants and cytokines at greater levels than other scaffolds, leading to the establishment of a vascular network. However, the scaffold degraded before this process was complete, and angiogenesis was not observed in the core regions of these scaffolds.

Following the same trend as cell density, the blood vessel density generally increased with implantation time, and progressed from the margins towards the center of the scaffold. Pieper *et al.* also observed the steady increase in the number of blood

vessels,[37] except between 4 and 10 weeks, where they observed a decrease in the number of blood vessels. These scaffolds were not harvested at 10 weeks, but a decrease in vessel density was seen at both the edge and core region of the crosslinked scaffolds, between Days 35 and 42. This may be explained in part by an increase in vessel size as they become more mature within the implant. Tiny capillaries eventually remodel to create larger vessels, reducing the total number of vessels, but not the amount of blood delivered. As blood vessels were measured here, no consideration was given to the size of the vessels.

The methods used to count blood vessels and generate data regarding the angiogenesis within the scaffolds, while it was applied consistently to allow comparisons between scaffold types, is not consistent with densities achieved in other collagen based implants. Generally, the results shown here are much lower than what has been previously reported for similar implants.[95,98] This may in part have to do with the detection method used to identify blood vessels. The shape and size of blood vessels vary greatly, and the actual shape observed in the microscope slide is further altered by the relative orientation of the vessel to the sectioning plane. Other studies have sometimes used immunohistochemistry to positively identify certain proteins that are found only within blood vessels, such as collagen-IV, CD31, or von Willebrand factor.[44] This would remove the dependence of the measurement on the shape and size of the vessel. While this has probably led to an underestimation of the total vascularity of these implants, the changes in blood vessel density and the relative amounts are accurate.

MRI measurements of blood flow in the scaffolds were performed using serial contrast-enhanced MRI to measure the time to maximum enhancement (time-to-peak,

TTP) and the time for the maximum enhancement to decrease to half of its peak value ($T_{1/2}$). These results showed that blood flow in the center of the scaffolds increased with increasing implantation time, consistent with the observed increase in vessel density. Crosslinked scaffolds had longer TTP and $T_{1/2}$ values than uncrosslinked scaffolds, suggesting reduced flow and lower blood vessel densities, opposite to the histology observations. However, these MRI measurements do not account for the shorter diffusion distances in the uncrosslinked scaffolds, due to their smaller size, which may explain this discrepancy.

6.2.4 Void Area

The void area of all scaffolds was found to decrease with postoperative time. This finding is consistent with expected results and previous studies that have shown collagen implants to gradually be filled with natural tissue.[10] However, the correlation between tissue ingrowth and void area is not seen in the literature to the best of the author's knowledge. Void area measurements may be considered the inverse of tissue ingrowth, except for the scaffold material present in the ROI. The implants are initially very porous (>90%)[15] and as they are remodeled and incorporated into the subcutaneous fascia, these pores are filled by the deposition of new ECM, angiogenesis and increasing cellular densities. The degradation of the implant also leads the breakdown of struts that maintain the individual pore volumes as the scaffold is remodeled.

EDC+CS scaffolds were completely filled with ECM and cells by Day 28, while the EDC scaffolds only showed similar filling by Day 35 and UnX scaffolds did not fill completely by Day 14. According to Pieper *et al*, the EDC+CS scaffolds still maintained their open porous structure at 10 weeks. This discrepancy could be due to a number of

factors. One possible explanation could be that the rats used in this study were much younger and their higher metabolisms/growth impacted the remodeling process.

A reversal in the gradient direction in crosslinked scaffolds, from low-to-high to high-to-low, when comparing edge to core void areas at early and late time points, respectively, is in part due to the initial formation of a dense capsule that is eventually remodeled during the tissue integration process. The final densities at the center of the crosslinked scaffolds were greater than the density of normal, homeostatic tissue.

These results for void areas are consistent with the measurements of cellular densities and blood vessels, which all capture different aspects of the remodeling process. The consistency between all three measurements provides strong evidence supporting the conclusion that better tissue response and ingrowth is observed in the EDC+CS scaffolds compared to the other two conditions.

T_2 and ADC measurements of the crosslinked scaffolds remained relatively constant at time points after 21 days, as observed in the void area measurements, showing good agreement between the two analysis modalities. Uncrosslinked scaffolds generally have lower void areas than crosslinked scaffolds, which was reflected in the lower ADC and T_2 values of these scaffolds.

6.3 MRI Correlations

The correlations between histology measurements of cellular density, void area, and scaffold thickness against MRI measurements of T_2, ADC, and scaffold volume show that there is a relationship between the two analysis modalities. The strongest correlation was seen between the average void areas and water T_2 relaxation times. This result makes sense, given that the T_2 value depends heavily on the ratio between free (bulk)

water molecules and bound water molecules. The binding of water to soluble proteins, cell membranes, and structural proteins all reduce the measured T_2 value. The void area is directly related to the amount of material available to bind water.

Attempts to use multiple linear regressions were unsuccessful. Presumably, using more than one MRI parameter to predict a histological measurement may give a better result as changes in the physiological state would influence all MRI parameters to some extent. However, the MRI parameters themselves are usually highly correlated. For example, short T_2 values are usually associated with slow ADC values. When performing multiple linear regressions, it is necessary to have no relationships between the independent variables. The slight linear trend in the residual values suggests that there is some dependence on implantation time that is not accounted for, or that a simple linear regression is not the most appropriate model. However, previous studies documenting the relationship between cellular density and ADC have used simple linear regressions.[73,74]

The relationship between total cellularity, T_2, and ADC values has been well documented in the literature.[72-74,99,100] Based on these previous results, it is expected that the correlations between the histological and MRI data in our study would be stronger. For example, one study reported a correlation coefficient of $r = -0.71$ between cell density and ADC in tumors. [74] In the present study, the differences in spatial resolution between the two analysis modalities may have also contributed to the weak correlations. The histological sections were five micrometers in thickness, whereas each MRI slice was one millimeter thick. This resulted in under-sampled histology data relative to the MRI data; which analyzed and averaged the whole volume of the scaffold.

While the scaffolds are assumed to be relatively homogenous in the direction perpendicular to the plane of the images, particularly in the central regions, this was not verified using multiple histology slices. Future studies should increase the number of histological sections analyzed per MRI slice to better correlate that data distributions associated with the sampling frequencies.

These correlations would also be improved by better co-registering the two data sets. This histological analysis samples a narrow region from the central MRI slice for each scaffold. Instead of comparing an average cellular density, computed by averaging across the thickness of a section, to an average T_2 value taken over the entire scaffold, it would be better to compare just the central region of an MRI slice with the histology section analyzed. The measurements from the binned histology regions could be averaged to cover the same spatial distance as an MR image pixel. Comparisons could then be made on a pixel by pixel basis. This would account for heterogeneity across the thickness of the scaffold and lead to better correlations.

7 Future Work

The statistically significant correlations between that two analysis modalities show that MRI can be used to faithfully monitor the remodeling of collagen scaffolds. The conclusions drawn from this study would be greatly strengthened by repeating the experiments to obtain independent histology samples at each time point. The differential tissue responses would be confirmed and the differences between the scaffolds can be statistically confirmed. This would also create a more complete histology dataset for more accurate correlations with the MRI dataset. Furthermore, using immunohistochemistry to positively identify blood vessels will lead to a more accurate measurement of the vascularity of the implants.

The differential tissue responses that were obtained by the various crosslinking treatments and conjugation of chondroitin sulfate to the scaffold could be further widened by implanting scaffolds with other treatments. Changing the GAG used to heparin sulfate or some other GAG would produce varying cellular responses. The incorporation of growth factors, such as bFGF[101] and VEGF[102] has also been shown to greatly alter the tissue response. These would both allow further histology and MRI data to be collected for correlations, advancing the understanding of how the two analysis modalities relate to each other.

The void area correlates well with T_2 values, however, in terms of physiology, void area is not a commonly used metric. Usually, total collagen content or new collagen deposition is measured in scaffolds to determine how well the implant is integrating with the host tissue. Using immunohistochemistry to stain for specific types of rat collagen (types I and III) within the bovine collagen scaffold will provide more data about how the

cells are responding. Large amounts of new collagen synthesis would suggest greater biocompatibility and a favorable cellular response. Related to this, bovine collagen antibodies would provide a better metric for scaffold degradation. Measuring the changes in actual material is better than measuring the size when multiple processes occur within that space.

8 Summary

This study has characterized the varying tissue responses observed when collagen scaffolds, crosslinked with EDC alone or in the presence of chondroitin sulfate, are implanted into dorsal subcutaneous pockets of rats and these data are correlated with MRI assessments of the scaffolds. The improved biostability of crosslinked scaffolds led to greater persistence of these scaffolds compared to uncrosslinked scaffolds. The addition of CS further increased the biostability of the scaffold. Greatest cellular density was observed in uncrosslinked scaffolds at Day 14. Crosslinked scaffolds took longer to populate with cells, and reach similar cellular densities after 35 days. An increased inflammatory response was thought to contribute to the greater cellular densities in uncrosslinked scaffolds, and was associated with a thicker capsule surrounding the implants. Measurements of blood vessel density showed the establishment of a vascular network within the EDC+CS scaffolds at 28 days and 35 days for the EDC scaffolds; indicating faster integration with the surrounding tissue is achieved by conjugating CS to the collagen scaffolds. The void area observations showed scaffold pores were gradually filled by new ECM deposition. EDC+CS scaffolds filled before the EDC scaffolds; again showing faster integration. Uncrosslinked scaffolds did not fill with ECM and blood vessels as completely as the crosslinked scaffolds. These observations are based on a limited number of samples, and care should be taken interpreting these data.

Correlations between the MRI and histology measurements showed that relationships existed between cell density and T_2 and ADC, and between void area and T_2 and ADC. The strongest correlation was observed between void area and T_2. These

results demonstrate that MRI is sensitive to physiological changes that occur during the remodeling of collagen implants.

9 References

1. Srinivasan A, Goyal M, Al Azri F, Lum C. State-of-the-art imaging of acute stroke. Radiographics 2006;26 Suppl 1:S75-95.
2. Gillies RJ, Bhujwalla ZM, Evelhoch J, Garwood M, Neeman M, Robinson SP, Sotak CH, Van Der Sanden B. Applications of magnetic resonance in model systems: tumor biology and physiology. Neoplasia 2000;2(1-2):139-151.
3. Bell E, Ehrlich HP, Buttle DJ, Nakatsuji T. Living tissue formed in vitro and accepted as skin-equivalent tissue of full thickness. Science 1981;211(4486):1052-1054.
4. Yannas IV, Burke JF, Orgill DP, Skrabut EM. Wound tissue can utilize a polymeric template to synthesize a functional extension of skin. Science 1982;215(4529):174-176.
5. Thomas AC, Campbell GR, Campbell JH. Advances in vascular tissue engineering. Cardiovasc Pathol 2003;12(5):271-276.
6. Steadman JR, Rodkey WG. Tissue-engineered collagen meniscus implants: 5- to 6-year feasibility study results. Arthroscopy 2005;21(5):515-525.
7. Friess W. Collagen--biomaterial for drug delivery. Eur J Pharm Biopharm 1998;45(2):113-136.
8. Pachence JM. Collagen-based devices for soft tissue repair. J Biomed Mater Res 1996;33(1):35-40.
9. Chvapil M. Collagen sponge: theory and practice of medical applications. J Biomed Mater Res 1977;11(5):721-741.
10. Bailey AJ. Perspective article: the fate of collagen implants in tissue defects. Wound Repair Regen 2000;8(1):5-12.
11. Liu X, Ma PX. Polymeric scaffolds for bone tissue engineering. Ann Biomed Eng 2004;32(3):477-486.
12. Hutmacher DW. Scaffold design and fabrication technologies for engineering tissues--state of the art and future perspectives. J Biomater Sci Polym Ed 2001;12(1):107-124.
13. Yannas IV, Lee E, Orgill DP, Skrabut EM, Murphy GF. Synthesis and characterization of a model extracellular matrix that induces partial regeneration of adult mammalian skin. Proc Natl Acad Sci U S A 1989;86(3):933-937.
14. Sachlos E, Czernuszka JT. Making tissue engineering scaffolds work. Review: the application of solid freeform fabrication technology to the production of tissue engineering scaffolds. Eur Cell Mater 2003;5:29-40.
15. O'Brien FJ, Harley BA, Yannas IV, Gibson L. Influence of freezing rate on pore structure in freeze-dried collagen-GAG scaffolds. Biomaterials 2004;25(6):1077-1086.
16. Schoof H, Apel J, Heschel I, Rau G. Control of pore structure and size in freeze-dried collagen sponges. J Biomed Mater Res 2001;58(4):352-357.
17. Kesting RE. Synthetic Polymeric Membranes: McGraw-Hill Inc; 1971.
18. Atiyeh BS, Gunn SW, Hayek SN. State of the art in burn treatment. World J Surg 2005;29(2):131-148.
19. Lynn AK, Yannas IV, Bonfield W. Antigenicity and immunogenicity of collagen. J Biomed Mater Res B Appl Biomater 2004;71(2):343-354.

20. Khor E. Methods for the treatment of collagenous tissues for bioprostheses. Biomaterials 1997;18(2):95-105.
21. Grabarek Z, Gergely J. Zero-length crosslinking procedure with the use of active esters. Anal Biochem 1990;185(1):131-135.
22. Olde Damink LH, Dijkstra PJ, van Luyn MJ, van Wachem PB, Nieuwenhuis P, Feijen J. In vitro degradation of dermal sheep collagen cross-linked using a water-soluble carbodiimide. Biomaterials 1996;17(7):679-684.
23. Instructions: EDC. Pierce Biotechnology, 2007. Electronic Source http://www.piercenet.com/files/0475as4.pdf Accessed: 5/15/2007.
24. Gratzer PF, Lee JM. Control of pH alters the type of cross-linking produced by 1-ethyl-3-(3-dimethylaminopropyl)-carbodiimide (EDC) treatment of acellular matrix vascular grafts. J Biomed Mater Res 2001;58(2):172-179.
25. Lee J, Edwards HHL, Pereira CA, Samii SI. Crosslinking of tissue-derived biomaterials in 1-ethyl-3-(3-dimethylaminopropyl)-carbodiimide (EDC). J Mater Sci Mater Med 1996;7:531-541.
26. Pieper JS, Oosterhof A, Dijkstra PJ, Veerkamp JH, van Kuppevelt TH. Preparation and characterization of porous crosslinked collagenous matrices containing bioavailable chondroitin sulphate. Biomaterials 1999;20(9):847-858.
27. 130672 N-Hydroxysuccinimide. Sigma-Aldrich, 2007. Electronic Source http://www.sigmaaldrich.com/catalog/search/ProductDetail/ALDRICH/130672 Accessed: 5/15/2007.
28. van Wachem PB, van Luyn MJ, Olde Damink LH, Dijkstra PJ, Feijen J, Nieuwenhuis P. Biocompatibility and tissue regenerating capacity of crosslinked dermal sheep collagen. J Biomed Mater Res 1994;28(3):353-363.
29. Lee CR, Grodzinsky AJ, Spector M. The effects of cross-linking of collagen-glycosaminoglycan scaffolds on compressive stiffness, chondrocyte-mediated contraction, proliferation and biosynthesis. Biomaterials 2001;22(23):3145-3154.
30. Everaerts F, Torrianni M, van Luyn M, van Wachem P, Feijen J, Hendriks M. Reduced calcification of bioprostheses, cross-linked via an improved carbodiimide based method. Biomaterials 2004;25(24):5523-5530.
31. Duan X, Sheardown H. Crosslinking of collagen with dendrimers. J Biomed Mater Res A 2005;75(3):510-518.
32. Zeeman R, Dijkstra PJ, van Wachem PB, van Luyn MJ, Hendriks M, Cahalan PT, Feijen J. Successive epoxy and carbodiimide cross-linking of dermal sheep collagen. Biomaterials 1999;20(10):921-931.
33. Docherty R, Forrester JV, Lackie JM, Gregory DW. Glycosaminoglycans facilitate the movement of fibroblasts through three-dimensional collagen matrices. J Cell Sci 1989;92 (Pt 2):263-270.
34. Schaefer T, Roux M, Stuhlsatz HW, Herken R, Coulomb B, Krieg T, Smola H. Glycosaminoglycans modulate cell-matrix interactions of human fibroblasts and endothelial cells in vitro. J Cell Sci 1996;109 (Pt 2):479-488.
35. Sasisekharan R, Raman R, Prabhakar V. Glycomics approach to structure-function relationships of glycosaminoglycans. Annu Rev Biomed Eng 2006;8:181-231.
36. Ferdous Z, Grande-Allen KJ. Utility and Control of Proteoglycans in Tissue Engineering. Tissue Eng 2007.

37. Pieper JS, van Wachem PB, van Luyn MJA, Brouwer LA, Hafmans T, Veerkamp JH, van Kuppevelt TH. Attachment of glycosaminoglycans to collagenous matrices modulates the tissue response in rats. Biomaterials 2000;21(16):1689-1699.
38. Von Recum A, Jacobi JE. Handbook of biomaterials evaluation : scientific, technical, and clinical testing of implant materials. Philadelphia, PA: Taylor & Francis; 1999. xix, 915 p.
39. Black J. Biological Performance of Materials: Fundamentals of Biocompatibility. New York, NY: Mercel Dekker, Inc.; 1999.
40. Chvapil M, Speer D, Mora W, Eskelson C. Effect of tanning agent on tissue reaction to tissue implanted collagen sponge. J Surg Res 1983;35(5):402-409.
41. Pieper JS, Hafmans T, van Wachem PB, van Luyn MJ, Brouwer LA, Veerkamp JH, van Kuppevelt TH. Loading of collagen-heparan sulfate matrices with bFGF promotes angiogenesis and tissue generation in rats. J Biomed Mater Res 2002;62(2):185-194.
42. van Wachem PB, Plantinga JA, Wissink MJ, Beernink R, Poot AA, Engbers GH, Beugeling T, van Aken WG, Feijen J, van Luyn MJ. In vivo biocompatibility of carbodiimide-crosslinked collagen matrices: Effects of crosslink density, heparin immobilization, and bFGF loading. J Biomed Mater Res 2001;55(3):368-378.
43. Patel ZS, Mikos AG. Angiogenesis with biomaterial-based drug- and cell-delivery systems. J Biomater Sci Polym Ed 2004;15(6):701-726.
44. van Amerongen MJ, Molema G, Plantinga J, Moorlag H, van Luyn MJ. Neovascularization and vascular markers in a foreign body reaction to subcutaneously implanted degradable biomaterial in mice. Angiogenesis 2002;5(3):173-180.
45. Silvestre JS, Mallat Z, Duriez M, Tamarat R, Bureau MF, Scherman D, Duverger N, Branellec D, Tedgui A, Levy BI. Antiangiogenic effect of interleukin-10 in ischemia-induced angiogenesis in mice hindlimb. Circ Res 2000;87(6):448-452.
46. Phongkitkarun S, Kobayashi S, Kan Z, Lee TY, Charnsangavej C. Quantification of angiogenesis by functional computed tomography in a Matrigel model in rats. Acad Radiol 2004;11(5):573-582.
47. Kobayashi H, Sato N, Kawamoto S, Saga T, Hiraga A, Ishimori T, Konishi J, Togashi K, Brechbiel MW. 3D MR angiography of intratumoral vasculature using a novel macromolecular MR contrast agent. Magn Reson Med 2001;46(3):579-585.
48. Kuriashkin IV, Losonsky JM. Contrast enhancement in magnetic resonance imaging using intravenous paramagnetic contrast media: a review. Vet Radiol Ultrasound 2000;41(1):4-7.
49. Woessner JF, Jr. Determination of Hydroxyproline in Connective Tissues. In: Hall DA, editor. The Methodology of Connective Tissue Research. First ed. Oxford: Joynson-Bruvvers Ltd; 1976. p 227-233.
50. Pek YS, Spector M, Yannas IV, Gibson LJ. Degradation of a collagen-chondroitin-6-sulfate matrix by collagenase and by chondroitinase. Biomaterials 2004;25(3):473-482.
51. Cahn F. Modification of Natural Polymers: Collagen-Glycosaminoglycan Copolymers. Methods of Tissue Engineering: Academic Press; 2002. p 515-523.

52. Loukas CG, Linney A. A survey on histological image analysis-based assessment of three major biological factors influencing radiotherapy: proliferation, hypoxia and vasculature. Comput Methods Programs Biomed 2004;74(3):183-199.
53. Liang HC, Chang Y, Hsu CK, Lee MH, Sung HW. Effects of crosslinking degree of an acellular biological tissue on its tissue regeneration pattern. Biomaterials 2004;25(17):3541-3552.
54. McKegney M, Taggart I, Grant MH. The influence of crosslinking agents and diamines on the pore size, morphology and the biological stability of collagen sponges and their effect on cell penetration through the sponge matrix. J Mater Sci Mater Med 2001;12(9):833-844.
55. Ma L, Gao C, Mao Z, Shen J, Hu X, Han C. Thermal dehydration treatment and glutaraldehyde cross-linking to increase the biostability of collagen-chitosan porous scaffolds used as dermal equivalent. J Biomater Sci Polym Ed 2003;14(8):861-874.
56. Marks MG, Doillon C, Silver FH. Effects of fibroblasts and basic fibroblast growth factor on facilitation of dermal wound healing by type I collagen matrices. J Biomed Mater Res 1991;25(5):683-696.
57. Kawai K, Suzuki S, Tabata Y, Ikada Y, Nishimura Y. Accelerated tissue regeneration through incorporation of basic fibroblast growth factor-impregnated gelatin microspheres into artificial dermis. Biomaterials 2000;21(5):489-499.
58. Smith RC. Understanding magnetic resonance imaging. Boca Raton: CRC Press LLC; 1997.
59. Haacke EM. Magnetic resonance imaging : physical principles and sequence design. New York: J. Wiley & Sons; 1999. xxvii, 914 p. p.
60. Constantinidis I, Sambanis A. Noninvasive Monitoring of Tissue-Engineered Constructs by Nuclear Magnetic Resonance Methodologies. Tissue Eng 1998;4(1):9-17.
61. Traore AS, Woerly S, Doan VD, Marois Y, Guidoin R. In vivo magnetic resonance imaging and relaxometry study of a porous hydrogel implanted in the trapezius muscle of rabbits. Tissue Eng 2000;6(3):265-278.
62. Ko IK, Song HT, Cho EJ, Lee ES, Huh YM, Suh JS. In vivo MR imaging of tissue-engineered human mesenchymal stem cells transplanted to mouse: a preliminary study. Ann Biomed Eng 2007;35(1):101-108.
63. Mader K, Bacic G, Domb A, Elmalak O, Langer R, Swartz HM. Noninvasive in vivo monitoring of drug release and polymer erosion from biodegradable polymers by EPR spectroscopy and NMR imaging. J Pharm Sci 1997;86(1):126-134.
64. Choi HY, Lee JS, Park HJ, Oum BS, Kim HJ, Park do Y. Magnetic resonance imaging assessment of fibrovascular ingrowth into porous polyethylene orbital implants. Clin Experiment Ophthalmol 2006;34(4):354-359.
65. Baird AE, Warach S. Magnetic resonance imaging of acute stroke. J Cereb Blood Flow Metab 1998;18(6):583-609.
66. Sparrow PJ, Kurian JB, Jones TR, Sivananthan MU. MR imaging of cardiac tumors. Radiographics 2005;25(5):1255-1276.
67. Schima W. MRI of the pancreas: tumours and tumour-simulating processes. Cancer Imaging 2006;6:199-203.
68. Taouli B, Losada M, Holland A, Krinsky G. Magnetic resonance imaging of hepatocellular carcinoma. Gastroenterology 2004;127(5 Suppl 1):S144-152.

69. Pagani E, Bammer R, Horsfield MA, Rovaris M, Gass A, Ciccarelli O, Filippi M. Diffusion MR imaging in multiple sclerosis: technical aspects and challenges. AJNR Am J Neuroradiol 2007;28(3):411-420.
70. Kan P, Liu JK, Hedlund G, Brockmeyer DL, Walker ML, Kestle JR. The role of diffusion-weighted magnetic resonance imaging in pediatric brain tumors. Childs Nerv Syst 2006;22(11):1435-1439.
71. Sotak CH. Nuclear magnetic resonance (NMR) measurement of the apparent diffusion coefficient (ADC) of tissue water and its relationship to cell volume changes in pathological states. Neurochem Int 2004;45(4):569-582.
72. Henning EC, Azuma C, Sotak CH, Helmer KG. Multispectral tissue characterization in a RIF-1 tumor model: monitoring the ADC and T2 responses to single-dose radiotherapy. Part II. Magn Reson Med 2007;57(3):513-519.
73. Hayashida Y, Hirai T, Morishita S, Kitajima M, Murakami R, Korogi Y, Makino K, Nakamura H, Ikushima I, Yamura M, Kochi M, Kuratsu JI, Yamashita Y. Diffusion-weighted imaging of metastatic brain tumors: comparison with histologic type and tumor cellularity. AJNR Am J Neuroradiol 2006;27(7):1419-1425.
74. Lyng H, Haraldseth O, Rofstad EK. Measurement of cell density and necrotic fraction in human melanoma xenografts by diffusion weighted magnetic resonance imaging. Magn Reson Med 2000;43(6):828-836.
75. Kiessling F, Morgenstern B, Zhang C. Contrast agents and applications to assess tumor angiogenesis in vivo by magnetic resonance imaging. Curr Med Chem 2007;14(1):77-91.
76. Kandasamy S. *In vivo* monitoring of collagen-sponge remodeling using MRI. Worcester: Worcester Polytechnic Institute. 2007. 88 p.
77. Institute of Laboratory Animal Resources (U.S.). Committee on Care and Use of Laboratory Animals. Guide for the care and use of laboratory animals. Bethesda, Md.: U.S. Dept. of Health and Human Services, Public Health Service; p v.
78. Barnes D. Research in the News: Spinal Cord Injury. National Institutes of Health (NIH), 2007. Electronic Source http://science.education.nih.gov/home2.nsf/Educational+Resources/Resource+Formats/Tutorials+&+Reviews/41B8971F1A21A38F85256CCD00631593 Accessed: 5/2/2007.
79. Rasband WS. ImageJ. Version 1.37. Bethesda, MD: National Institutes of Health; 1997-2006.
80. Thevenaz P, Unser M. User-friendly semiautomated assembly of accurate image mosaics in microscopy. Microsc Res Tech 2007;70(2):135-146.
81. Sharkawy AA, Klitzman B, Truskey GA, Reichert WM. Engineering the tissue which encapsulates subcutaneous implants. I. Diffusion properties. J Biomed Mater Res 1997;37(3):401-412.
82. Caruso AB, Dunn MG. Functional evaluation of collagen fiber scaffolds for ACL reconstruction: cyclic loading in proteolytic enzyme solutions. J Biomed Mater Res A 2004;69(1):164-171.
83. Angele P, Abke J, Kujat R, Faltermeier H, Schumann D, Nerlich M, Kinner B, Englert C, Ruszczak Z, Mehrl R, Mueller R. Influence of different collagen species on physico-chemical properties of crosslinked collagen matrices. Biomaterials 2004;25(14):2831-2841.

84. Mi FL, Shyu SS, Peng CK, Wu YB, Sung HW, Wang PS, Huang CC. Fabrication of chondroitin sulfate-chitosan composite artificial extracellular matrix for stabilization of fibroblast growth factor. J Biomed Mater Res A 2006;76(1):1-15.
85. Mao JS, Liu HF, Yin YJ, Yao KD. The properties of chitosan-gelatin membranes and scaffolds modified with hyaluronic acid by different methods. Biomaterials 2003;24(9):1621-1629.
86. Pieper JS, Hafmans T, Veerkamp JH, van Kuppevelt TH. Development of tailor-made collagen-glycosaminoglycan matrices: EDC/NHS crosslinking, and ultrastructural aspects. Biomaterials 2000;21(6):581-593.
87. Anderson JM, Cook G, Costerton B, Hanson SR, Pettersen-Hensten A, Jacobsen N, Johnson RJ, Mitchell RN, Pasmore M, Schoen FJ, Shirtliff M, Stoodley P. Host Reactions to Biomaterals and Their Evaluation. In: Ratner BD, editor. Biomaterials Science. 2nd ed. San Diego: Elsevier Academic Press; 2004. p 293-354.
88. Chakraborti S, Mandal M, Das S, Mandal A, Chakraborti T. Regulation of matrix metalloproteinases: an overview. Mol Cell Biochem 2003;253(1-2):269-285.
89. Bali JP, Cousse H, Neuzil E. Biochemical basis of the pharmacologic action of chondroitin sulfates on the osteoarticular system. Semin Arthritis Rheum 2001;31(1):58-68.
90. Nehrer S, Breinan HA, Ramappa A, Hsu HP, Minas T, Shortkroff S, Sledge CB, Yannas IV, Spector M. Chondrocyte-seeded collagen matrices implanted in a chondral defect in a canine model. Biomaterials 1998;19(24):2313-2328.
91. Ellis DL, Yannas IV. Recent advances in tissue synthesis in vivo by use of collagen-glycosaminoglycan copolymers. Biomaterials 1996;17(3):291-299.
92. Doillon CJ, Wasserman AJ, Berg RA, Silver FH. Behaviour of fibroblasts and epidermal cells cultivated on analogues of extracellular matrix. Biomaterials 1988;9(1):91-96.
93. Smith SM, West LA, Govindraj P, Zhang X, Ornitz DM, Hassell JR. Heparan and chondroitin sulfate on growth plate perlecan mediate binding and delivery of FGF-2 to FGF receptors. Matrix Biol 2007;26(3):175-184.
94. Urenjak J, Williams SR, Gadian DG, Noble M. Proton nuclear magnetic resonance spectroscopy unambiguously identifies different neural cell types. J Neurosci 1993;13(3):981-989.
95. Lai PH, Chang Y, Chen SC, Wang CC, Liang HC, Chang WC, Sung HW. Acellular biological tissues containing inherent glycosaminoglycans for loading basic fibroblast growth factor promote angiogenesis and tissue regeneration. Tissue Eng 2006;12(9):2499-2508.
96. Shintani Y, Takashima S, Asano Y, Kato H, Liao Y, Yamazaki S, Tsukamoto O, Seguchi O, Yamamoto H, Fukushima T, Sugahara K, Kitakaze M, Hori M. Glycosaminoglycan modification of neuropilin-1 modulates VEGFR2 signaling. Embo J 2006;25(13):3045-3055.
97. Tonnesen MG, Feng X, Clark RA. Angiogenesis in wound healing. J Investig Dermatol Symp Proc 2000;5(1):40-46.
98. Kidd KR, Dal Ponte DB, Kellar RS, Williams SK. A comparative evaluation of the tissue responses associated with polymeric implants in the rat and mouse. J Biomed Mater Res 2002;59(4):682-689.

99. Helmer KG, Meiler MR, Sotak CH, Petruccelli JD. Comparison of the return-to-the-origin probability and the apparent diffusion coefficient of water as indicators of necrosis in RIF-1 tumors. Magn Reson Med 2003;49(3):468-478.
100. Ahn JM, Yoon HK, Suh YL, Kim EY, Han BK, Yoon JH, Kim SH, Cho JM, Kim SM, Kang HS. Infantile fibromatosis in childhood: findings on MR imaging and pathologic correlation. Clin Radiol 2000;55(1):19-24.
101. Sabini P, Sclafani AP, Romo T, 3rd, McCormick SA, Cocker R. Modulation of tissue ingrowth into porous high-density polyethylene implants with basic fibroblast growth factor and autologous blood clot. Arch Facial Plast Surg 2000;2(1):27-33.
102. Nillesen ST, Geutjes PJ, Wismans R, Schalkwijk J, Daamen WF, van Kuppevelt TH. Increased angiogenesis and blood vessel maturation in acellular collagen-heparin scaffolds containing both FGF2 and VEGF. Biomaterials 2007;28(6):1123-1131.

10 Appendices

These appendices contain the ImageJ code that was used to consistently count cells and measure the void area fractions.

10.1 Cellular Density

```
macro "Cell Count [f5]"{
      run("HSB Stack Splitter");
      run("Subtract Background...", "rolling=50 white");
      run("Enhance Contrast", "saturated=0.5");
      run("Apply LUT");
      //run("Threshold...");
      setThreshold(0, 150);
      run("Convert to Mask");
      run("Watershed");
      run("Analyze   Particles...",   "size=5-200   circularity=0.40-1.00
show=Outlines display exclude summarize");
}
```

10.2 Void Area

```
macro "Void Fraction [f7]"{
      run("HSB Stack Splitter");
      run("Subtract Background...", "rolling=50 white");
      //run("Threshold...");
      setThreshold(250, 255);
      run("Convert to Mask");
      run("Measure");
}
```